

---

# **Preparing next generation tweezer systems for quantum simulation of spin models**

**Robin Eberhard**

---



Munich 2020



---

# **Vorbereitung einer neuer Generation optischer Tweezer zur Quantensimulation von Spin-Modellen**

---

Masterarbeit an der Fakultät für Physik  
Ludwig-Maximilians-Universität München  
Max-Planck-Institut für Quantenoptik

vorgelegt von

**Robin Eberhard**

München, den 16. Oktober 2020



# Preparing next generation tweezer systems for quantum simulation of spin models

Robin Eberhard

**Abstract** This thesis presents systems towards quantum manybody effects. Part of these are acousto-optically deflected tweezers, in order to dynamically move atoms. Two implementations for the tweezers are discussed, where for one, atoms are rearranged to deterministically achieve 100% filling across a tweezer grid, allowing to study correlations in more detail. Moreover, the dynamic tweezers allow for a spin-selective imaging approach, where a spin-sensitive laser beam traps only one spin state and moves it away from the other, thereby identifying the spin based on an image. Moreover, a system is discussed to increase the power available during loading of atoms into tweezers, ultimately paving the way to increase the available number of tweezers.



# Contents

<b>1. Introduction</b>	<b>1</b>
<b>2. Loading atoms into optical tweezers</b>	<b>3</b>
2.1. Theory on Polarization . . . . .	4
2.2. Electro-optical modulators . . . . .	6
2.2.1. Pockels effect . . . . .	6
2.2.2. Driving a Pockels cell . . . . .	9
2.2.3. Testing and evaluating pockels cells . . . . .	10
<b>3. Sorting of atoms</b>	<b>15</b>
3.1. Acousto-optically deflected tweezers . . . . .	15
3.1.1. Acousto-optical effect . . . . .	16
3.1.2. Preparation of the tweezers beams . . . . .	19
3.1.3. Moving tweezers . . . . .	22
3.1.4. Tweezer homogeneity . . . . .	22
3.2. Sorting algorithms . . . . .	24
3.2.1. Pathfinding . . . . .	25
3.2.2. Compression . . . . .	26
3.2.3. Comparison of the two algorithms . . . . .	27
3.3. Driving an RF-synthesizer for arbitrary pattern generation . . . . .	29
3.3.1. Functionality of the Spectrum driver . . . . .	32
3.3.2. Limits of using the card in the experiment . . . . .	34
3.4. Conclusion . . . . .	37
<b>4. State selective light shifts for spin-sensitive imaging</b>	<b>39</b>
4.1. Approaches . . . . .	39
4.1.1. Zeemann induced potential separation . . . . .	40
4.1.2. Utilization of state selective light shifts . . . . .	42
4.2. Setup . . . . .	46
4.2.1. Laser classification . . . . .	47

4.2.2. Beam setup of spin-selective laser . . . . .	47
4.2.3. Cavity classification . . . . .	49
<b>5. Conclusion and Outlook</b>	<b>53</b>
<b>A. Linear laser design</b>	<b>55</b>
<b>B. Cavity for frequency stability of spin-sensitive tweezer</b>	<b>57</b>
<b>C. PDH lock of cavity</b>	<b>59</b>
<b>Acknowledgements</b>	<b>61</b>

# 1. Introduction

Quantum mechanics has expanded the scope of physics, where a new way of thinking about atomic and photonics models emerged and new theories of microscopic effects are still researched experimentally and theoretically. Nowadays, within the realm of quantum research, atoms are being controlled in an isolated environment, that have allowed to set e.g. new high-precision time standards [1] and resolve new types of matter [2, 3]. The scope of these studies has greatly expanded over the last 30 years, as laser-cooling, trapping, and detection techniques have gained momentum. Within this realm, the field of quantum simulation is of particular interest to this thesis, where microscopic effects found in solid state physics are modelled by arranging and interacting atoms on a scale much larger than they appear in nature and can therefore be studied in detail. Forming the structures necessary to measure effects in this macroscopic regime, such as Ising [4] or Hubbard [5] models, is achieved by confining atoms to periodic potential wells in optical lattices.

Advancements in detection of atoms have led to quantum gas microscopes [6, 7], where single-site resolution in these lattices is possible and are thus a perfect fit for use in quantum simulators, as interactions and correlations between atoms can be studied in detail. This has allowed to measure e.g. superfluid to Mott insulator transitions [7] or antiferromagnetic correlations [5]. However, control over these systems was limited in the past, as optical lattices have a fixed geometry and cycle times were long due to the necessity of cooling atoms to ultra-cold temperatures. More recently however, optical tweezers have emerged [8–11], where each lattice site is generated from an individual laser beam. This allows high control and tunability not only between lattice sites, but also poses the ability to generate arbitrary geometries. As these traps can be made sufficiently deep, this removes the requirement of cooling atoms to ultra-cold temperatures, resulting in fast cycle times.

To study manybody effects in these optical tweezers, Rydberg atoms can be employed. They offer the ability of long-range interactions on a micrometer scale [12] and therefore across multiple tweezers. Direct manybody-effects are seen as part of the Rydberg blockade, where within a certain radius, only a single atom can be excited into a Rydberg state. However Rydberg atoms are very well suited to study spin Hamiltonians, which are used

to research quantum magnetism [13]. In combination with optical tweezers, coherent dynamics can be observed, as the positions of atoms aren't random. This has allowed for example, to observe coherent excitation hopping in spin-flip Hamiltonians [14] and large arrays of Rydberg atoms modelling Ising dynamics [15]. In another approach, out-of-time order correlators are a measure of chaotic behaviour in condensed matter physics and can be modelled in spin-like systems [16]. Quantum manybody dynamics in spin-models have also been observed using a programmable 1D quantum simulator, where symmetry breaking across phase transitions was detected [17].

This forms the building blocks for the experiment this thesis is a part of. Hereby, single Potassium-39 atoms are trapped in optical tweezers and excited to Rydberg levels [18]. The tweezers are generated through spatial light modulators (SLMs) [19], where arbitrary intensity patterns are formed and projected onto the atomic cloud.

This work presents three new setups towards this experiment. In Chapter 2, loading of potassium atoms from the cloud into tweezers is discussed. The chapter places focus on the theory behind electro-optical modulators (EOMs) which is followed by the characterization of two EOMs, that will be used to improve the loading stage of the experiment and allow deploying more tweezers in the future. Chapter 3 then works towards enabling unity filling in a grid of atoms. For this, a new way of generating the tweezers is introduced in the form of acousto-optical deflectors (AODs), which can move atoms into vacancies in the lattice. Therefore the theory behind the deflectors is explained and is followed by comparing two algorithms of achieving this sorting of atoms. The chapter is then concluded by describing the driver used for the dynamic tweezers and ways to work around its limitations. Finally, Chapter 4 presents a spin-selective imaging approach by applying dynamic tweezers that are sensitive to only one spin species using the same AODs as above. The spin-sensitive laser used in this setup was built during this thesis and is concluded with the characterization of this laser.

## 2. Loading atoms into optical tweezers

The experiment uses spatial light modulators (SLMs) to generate two-dimensional arrays of tweezers, which trap single atoms [19]. SLMs allow to generate various geometries, and therefore freely adjustable inter-atomic distances and trapping depths. However, in order to load atoms into the optical tweezers, they have to undergo several cooling stages first. Being vaporized from a solid sample of  $^{39}\text{K}$ , the atoms are decelerated by passing through a Zeeman-slower, which cools the atoms longitudinally. The atoms are then trapped, compressed and cooled in a magneto-optical trap (MOT) in the center of the vacuum chamber. The temperature limit in the MOT is the Doppler limit, therefore the sub-doppler techniques gray molasses [20] and red molasses are used in order to cool even further. When the atoms are cold enough, they are then loaded into the SLM tweezers. However, as the tweezers (at  $\lambda = 1064\text{ nm}$ ) are highly detuned to the D2 line (at  $\lambda_{D2} = 766.701\text{ nm}$ ), loading directly from the molasses proves difficult, due to the large light shifts of the D2 excited state of Potassium, making it highly anti-trapped. To overcome this issue, trapping and cooling beams can be temporarily alternated [21]. This way, cooling and trapping are never on at the same time and therefore heating due to light shifts is eliminated, as there are no excited atoms during the trapping phase. However, for this to work, the frequency of alternating the beams has to be much larger than the trapping frequency and therefore, the atoms see an effective, averaged trap.

So far, alternating between molasses cooling and trapping light, called chopping, is implemented using acousto-optical modulators (AOMs). However, the maximum switching speed of an AOM is limited by the speed of sound in the medium (here,  $\text{TeO}_2$  has  $4.2\text{ mm }\mu\text{s}^{-1}$ ) and results in a maximum chopping frequency of 1.4 MHz, governed by the AOM with the slowest rise time, which can be seen in Figure 2.1. By increasing the chopping frequency, the atoms heat less during each trapping cycle. As already mentioned, the atoms only see an averaged trap given by the duty cycle of the trapping beam. Thus, the pulse shape determines how much trapping power the atoms see. Improving therefore the pulse shape leads to more laser power that can be used per tweezer. This in turn means, more tweezers can be deployed, as the average power increases when the pulse shape is

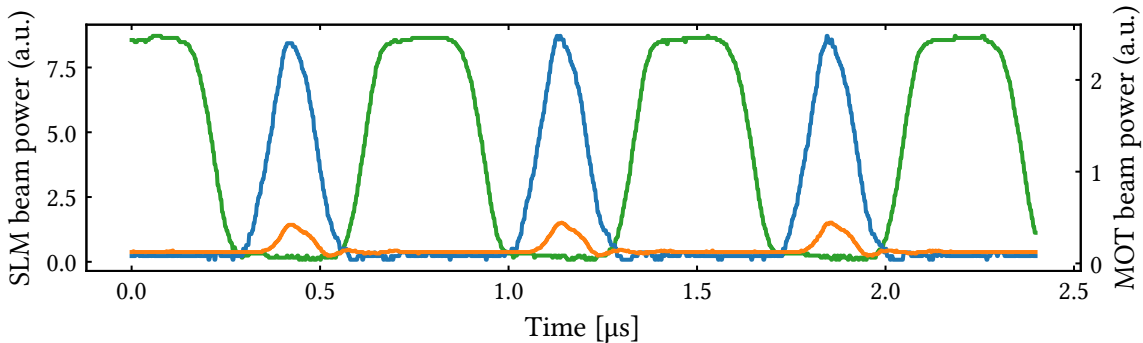


Figure 2.1.: Chopping in the experiment: MOT (cooler (blue), repumper (orange)) and SLM tweezer (green) beams alternate in the chopping sequence. The amplitude of the MOT beams is limited due to the risetime of the AOMs. The scale of the MOT beam amplitudes has been adjusted to match the SLM tweezer scale for better visualization.

more rectangular. Figure 2.1 shows how the pulse shape is limiting the average power during the cooling cycle as well as during trapping.

Achieving larger duty cycles and higher chopping frequencies is possible by using EOMs, which are not limited by acoustic waves. The optical medium is modulated using electric fields, and therefore switching speeds are only limited by their capacitance. Light entering the modulator will have its polarization turned, depending on the electric field that is applied. In the following, the polarization of electro-magnetic waves is briefly discussed, which is followed by the main effect governing the devices tested in this thesis – the Pockels effect. The devices are then evaluated by filtering one polarization component and by measuring the intensity of the light after the filter, the rise times and extinction ratio are determined. The new system allows to switch with rise times on the order of nanoseconds, improving the current system by at least two orders of magnitude.

## 2.1. Theory on Polarization

Switching laser beams using EOMs means turning and filtering the polarization of the light. Therefore in this subsection, the theory behind polarized monochromatic electromagnetic waves, leading to the Pockels effect governing EOMs is discussed.

Polarization of electromagnetic waves is understood as the orientation of their electric field in space, transverse to the direction of movement. In general, the electric field travelling

along the z-axis can be oriented somewhere in the x-y plane. Therefore, writing the electric field component of the light in this basis takes the following form:

$$\mathbf{E}(\mathbf{x}, t) = E_x \cos(kx - \omega t + \phi_x) \mathbf{e}_x + E_y \cos(ky - \omega t + \phi_y) \mathbf{e}_y. \quad (2.1)$$

Here,  $k$  and  $\omega$  refer to the wave number and angular frequency respectively. Depending on the amplitudes  $E_x$  and  $E_y$  and the phases  $\phi_x$  and  $\phi_y$ , the light can be in different polarization states. If it is not possible to write the electric field in this basis, then the light is not in a pure polarization state. Otherwise, it is **linear**, when either one of the amplitudes  $E_x$  or  $E_y$  is zero or when the phase difference  $\Delta\phi = \phi_x - \phi_y$  evaluates to 0 or  $\pi$ . It is **circular**, when the phase difference  $\Delta\phi = \pm\pi/2$  and the amplitudes are the same,  $E_x = E_y$ . In any other case, the wave is **elliptically** polarized.

Changing the phases of the  $x$  and  $y$  field component relative to each other gives the ability to influence the polarization. Light traversing a medium will accumulate a phase shift, depending on the refractive index, which affects the speed of light in the medium. Therefore, media that have different refractive indices  $n_x, n_y$  along the two axes  $x$  and  $y$  changes the relative phases of the electric field:

$$\phi_x(z) = k_0 n_x z \quad (2.2)$$

$$\phi_y(z) = k_0 n_y z \quad (2.3)$$

where  $k_0$  is the free space wave vector of the electric field component. Then a device that retards the phase difference  $\Delta\phi$  by  $\pi/2$ , which is a quarter of the wavelength, can change linearly polarized light to circularly polarized light (or vice-versa) and is therefore called a  $\lambda/4$  waveplate. Similarly, if the phase difference is changed by  $\Delta\phi = \pi$ , or a half wavelength, then we can turn linear polarization around a given axis or change the orientation of circularly polarized light. This is then called a  $\lambda/2$  waveplate. In the experiment, linearly polarized light enters the EOM, which will act as a  $\lambda/2$  waveplate, turning the polarization by  $90^\circ$ , making it easy to filter unwanted polarization components and switching the light on and off.

## 2.2. Electro-optical modulators

Light travelling through a material generally has a speed smaller than the speed of light, given by dividing the speed of light in vacuum by the material-dependent refractive index. Materials can change their refractive index by being exposed to an electric field, which in EOMs is generally a crystal between two electrodes. The electro-optical effect discussed in the following is the Pockels effect and applies, when the refractive index changes linearly with the electric field, at which point the EOM is called a Pockels cell. The effect is discussed in the following and the Pockels cells evaluated afterwards.

### 2.2.1. Pockels effect

As motivated in the previous section, the goal of modulating the light polarization is to change the phase difference of the electric field component when light traverses a medium. Following the argumentation from the book Fundamentals of Photonics [22], the Pockels effect can be described by evaluating the refractive index with respect to the electric field applied to the modulator. Writing this as  $n(E)$  and applying a Taylor expansion, we get the following expression:

$$n(E) = n_0 + \frac{dn}{dE} E + \mathcal{O}(E^2) \quad (2.4)$$

The Pockels effect is the linear dependence of the refractive index to the electric field, therefore higher orders are neglected. The prefactor  $dn/dE$  relates to the change of electric impermeability  $\Delta\eta$ , which is the ability of a material to be penetrated by an electromagnetic field. From

$$\eta = \frac{1}{n^2} \quad (2.5)$$

$$\frac{d\eta}{dn} \approx -\frac{2}{n_0^3} \quad (2.6)$$

$$\Delta n = \frac{dn}{dE} E, \quad (2.7)$$

we get

$$\Delta\eta = \frac{d\eta}{dn} \Delta n \approx -\frac{2}{n_0^3} \frac{dn}{dE} E = \mathfrak{r} E. \quad (2.8)$$

This results in the quantity  $\tau = -\frac{2}{n_0^3} \frac{dn}{dE}$ , which is called the Pockels coefficient given in units of  $\text{m V}^{-1}$ . It can be measured by evaluating the refractive index of the material:

$$n(E) = n_0 - \frac{1}{2}\tau n_0^3 E. \quad (2.9)$$

As was seen in Equations 2.2 and 2.3, the refractive index directly affects the phase shift, which in turn changes the polarization of the light wave. Combining this result with Equations 2.2 and 2.3 leads to an equation using parameters typically found in EOMs:

$$\begin{aligned} \phi &= k_0 L n \\ &= k_0 L n_0 - \frac{k_0}{2} L \tau n_0^3 E \\ &= \phi_0 - \frac{k_0}{2} L \tau n_0^3 E \\ &= \phi_0 - \frac{\pi}{\lambda_0} L \tau n_0^3 E \end{aligned} \quad (2.10)$$

where the relation  $k_0 = 2\pi/\lambda_0$  of the wave number was used.

In this application, the Pockels cells act as dynamic wave retarders. Given results from Section 2.1 we can tune the phase difference  $\Delta\phi = \phi_x - \phi_y$  along the axes  $x$  and  $y$  by applying an electric field along one of the axes. With the correct parameters, the phase difference lets the EOM act as a  $\lambda/2$  or  $\lambda/4$  waveplate. The following relations will help find the main formula governing Pockels cells, resulting in the voltage that needs to be applied to the EOM in order to turn the polarization by a given amount.

By labeling the refractive index in two dimensions as:

$$n_x(E) = n_{0,x} - \frac{1}{2}\tau_x n_{0,x}^3 E \quad (2.11)$$

$$n_y(E) = n_{0,y} - \frac{1}{2}\tau_y n_{0,y}^3 E, \quad (2.12)$$

the phase difference becomes:

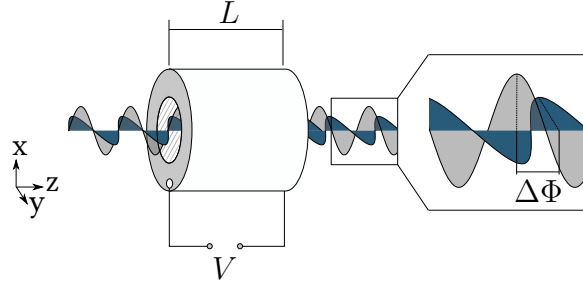


Figure 2.2.: Schematic view of light passing through an EOM with length  $L$ . The electrodes are positioned on the front and back side of the modulator, the same faces the light enters and exits. The light exiting the EOM has a relative phase shift  $\Delta\Phi$  depending on the change of refractive index due to the applied voltage  $V$ .

$$\Delta\phi = \phi_{0,x} - \phi_{0,y} - \frac{\pi}{\lambda_0} EL \left( \mathfrak{r}_x n_x^3 - \mathfrak{r}_y n_y^3 \right) \quad (2.13)$$

$$\Delta\phi = \Delta\phi_0 - \frac{\pi}{\lambda_0} EL \left( \mathfrak{r}_x n_x^3 - \mathfrak{r}_y n_y^3 \right). \quad (2.14)$$

The next step is to replace the electric field by a voltage that can be applied to the Pockels cell. For this, two electrodes are connected to the electro-optical material, separated by a distance  $d$ , giving the electric field as  $E = V/d$ . This quantity is replaced in Equation 2.14. By realizing that the phase is unitless, all other prefactors of the voltage can be combined into one quantity, called the half-wave voltage  $V_\pi$ :

$$V_\pi = \frac{d}{L} \frac{\lambda_0}{\mathfrak{r}_x n_x^3 - \mathfrak{r}_y n_y^3}. \quad (2.15)$$

Thus, the phase difference can be rewritten as:

$$\Delta\phi = \Delta\phi_0 - \pi \frac{V}{V_\pi}. \quad (2.16)$$

Therefore, applying the voltage  $V_\pi$ , the Pockels cell will act as a  $\lambda/2$  waveplate. A visual representation of the modulator and the light passing through it is given in Figure 2.2, highlighting the change in relative phase of the two components of the electro-magnetic wave.

We have seen, how applying a voltage to an electro-optical medium changes the refractive index and therefore affects the phase of an electromagnetic wave. By having two refractive indices in two axes, whose relative change depends on the applied voltage, it is therefore possible to modify the circularity and linearity of the polarization in an electro-optical modulator.

### 2.2.2. Driving a Pockels cell

With an understanding of the Pockels effect governing the EOMs tested in this thesis, the next step is driving the Pockels cells with the voltages used for switching. As the rise and fall times of the switched Pockels cells are crucial and depend only on the speed of applying the electric field, it is important to build electronics that can provide these fast rise and fall times. However, materials suitable for use as EOMs, such as  $\beta$ -bariumborate (BBO) and rubidium tanyl phosphate (RTP) have half-wave voltages in the kilovolt-regime, meaning not only does the hardware have to switch on fast timescales, but it also needs to be able to handle high voltages.

The Pockels cell drivers discussed in the following (by BME Bergmann) fulfill these requirements. Moreover, it contains viewports for the laser light, such that the Pockels cell can be integrated into the driver to not expose the high voltage to any parts of the experiment but the modulators. The driver has an input for the high voltage and option for watercooling in order to compensate temperature instabilities on the Pockels cell. Furthermore, it contains four inputs, that allow to have full control over the switching of the voltages. This means, the EOMs can be switched on and off by applying TTL signals to the inputs of the driver.

In order to correctly drive the Pockels cell and therefore turn the polarization of the light, it is necessary to understand the switching logic used inside the driver. Schematically, the driver is divided into the four switches mentioned above, that are controlled from the user: ON A, ON B, OFF A and OFF B. Two switches are connected to either side (labeled A and B) of the Pockels cell, such that A controls one electrode and B the other. Most importantly, the ON X and OFF X (X referring to either A or B) switches work exclusively, so sending a high to ON X also sends a low to OFF X and vice-versa. It is then possible to apply either a positive high voltage or a negative high voltage, depending on the state of the switches. For full identification of the circuit, which is given in Figure 2.3, the side containing the positive voltage information is called high side and similarly the side containing the negative voltage information is called low side. The figure shows switching logics for two different drives used in the experiment. These are named by the manufacturer as dpp-type and bpp-type and are to be used for the RTP and BBO Pockels cells respectively.

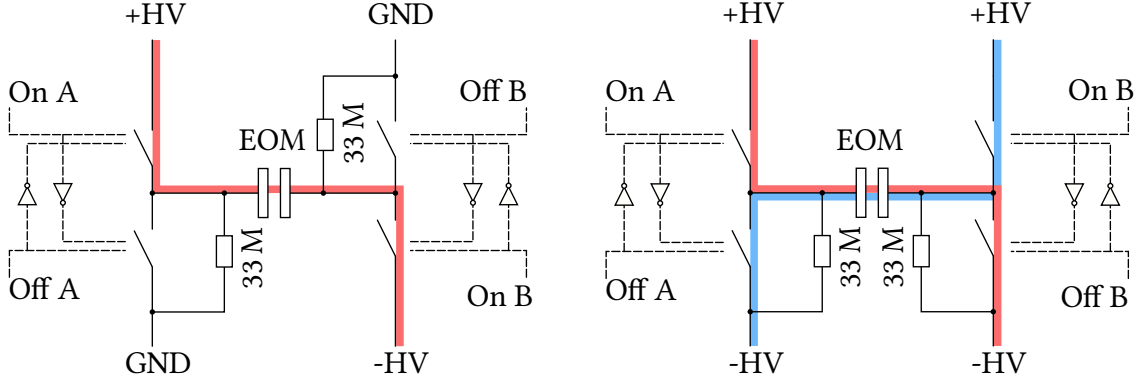


Figure 2.3.: Schematic of the high voltage switches used inside the bpp-type (left) and dpp-type (right) Pockels cell driver from BME Bergmann. Not-Gates on both A and B sides ensure that there is always a potential over the Pockels cell. The blue and red paths indicate the connection to apply a positive and negative voltage over the Pockels cell respectively.

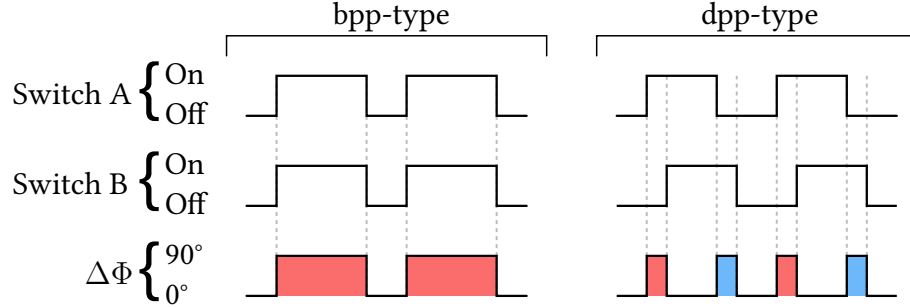


Figure 2.4.: Timing diagrams for the Pockels cell drivers to turn the polarization of the EOM  $90^\circ$ . The shaded areas show positive (red) and negative (blue) voltages applied to the pockels cells.

As motivated before, light will enter the EOM perfectly horizontally or vertically. Therefore, it is in theory possible, to apply either positive or negative half-wave voltages and therefore turn the polarization either way by  $90^\circ$ . The driver of the RTP pockels cell provides this feature and it will be used, as it results in higher performance, as is shown later. On the other hand, the BBO pockels cell already performs quite well and therefore does not need to be provided with alternating voltages. Figure 2.4 shows the timing diagrams necessary to apply to the driver inputs, which in turn directly affects the polarization of the light, as the EOM receives the half-wave voltage.

### 2.2.3. Testing and evaluating pockels cells

Two pockels cells (from Leysop Ltd.) are characterized in the following. The EOMs in contrast to the AOMs implemented in the current setup allow longer duty cycles of the tweezer

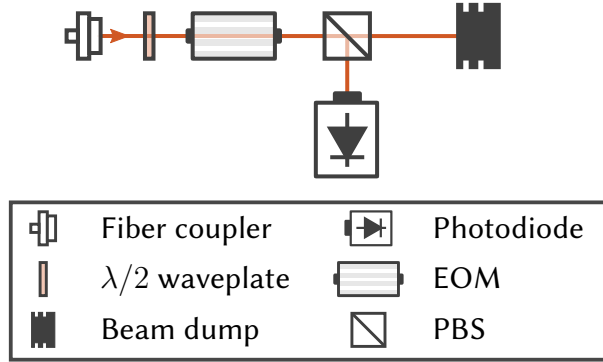


Figure 2.5.: The efficiency of the EOMs were evaluated by setting the polarization of the incoming light either horizontal or vertical using the waveplate. The Pockels cell will then periodically turn the polarization 90°, which can be seen by measuring the voltage on the photodiode.

light. Switching laser light is achieved in Pockels cells by exploiting the fact, that one linear polarization component can be filtered out by polarizers. In the following, a polarizing beam splitter (PBS) acts as the filter directly after the modulator as seen in Figure 2.5. This way, the setup can be configured such that applying no voltage means light passes through the beam splitter, while applying  $V_\pi$  means the light gets reflected 90° off the beam splitter, save for a fraction of light, given by the extinction ratio of the beam splitter (typically for the ones used in the experiment, manufactured by Thorlabs, the extinction ratio is about 1000:1).

Two Pockels cells were characterized by placing a photodiode on one end of the beam splitter. The EOMs are labeled by the material of their nonlinear crystal, RTP and BBO. Their characteristics are summarized in Table 2.2.3, where half wave voltages is given for 1064 nm light. Both EOMs are used in the chopping condition discussed earlier, where the RTP crystal will be used for the 770 nm and the BBO for the 1064 nm tweezer light.

First of all, the rise and fall times of the EOMs are determined. Light whose polarization component was filtered through the PBS arrives at the photodiode. For sufficiently high bandwidths on the photodiode and oscilloscope, the flanks of the signal are resolved and the rise time can be evaluated by fitting the function

$$f(x) = \frac{U_h}{1 + \exp(-x/\tau)} + U_l, \quad (2.17)$$

where  $U_h$  and  $U_l$  refer to the high and low voltage level of the signal respectively, which will come in useful later when evaluating the extinction ratio. The signals in Figure 2.6

	RTP	BBO
Aperture (crystal dimensions)	3 mm	3 mm
Total crystal length (2 crystals)	30 mm	50 mm
Approximate half wave voltage (1064nm)	1.0 kV	2.8 kV
Peak damage threshold (1064nm, 1ns pulse)	$> 1 \text{ GW cm}^{-2}$	$> 1 \text{ GW cm}^{-2}$
Insertion loss	$< 2 \%$	$< 1.5 \%$

Table 2.1.: Characteristics of the two Pockels cells with their respective non-linear crystal materials being RTP and BBO given from the datasheet of the manufacturer. The aperture, damage threshold and insertion loss are given for future reference.

were recorded for both EOMs, however, the fit can't be applied to the data, as the sampling rate is too low. Moreover, harmonics appear when the signal has risen to the upper level, indicating that the bandwidth of either the photodiode or the oscilloscope is too low. For this measurement, the oscilloscope (Teledyne Lecroy Wafesurfer 510) has a bandwidth of 1 GHz. The photodiode is a home-built model, whose bandwidth is limited by the built-in operational amplifier (OPA211) to around 45 MHz. Even though the sampling rate is too low, an upper bound for the rise time can still be given by measuring the distance between the last point on the lower level and the first point on the upper level. For both crystals, this means that the rise time is at least a fraction of a microsecond. In contrast to the AOMs that are currently in use, this is already an improvement by at least one order of magnitude (see Figure 2.1).

However, the manufacturer of the Pockels cell driver has done independent tests on the same EOMs used here. The data is available on their website [23] and they measured rise times for RTP and BBO as 3 ns and 4 ns respectively, which therefore improves on the AOM setup by three orders of magnitude in rise times.

Another important parameter is the extinction ratio, which is the amount of light that is left, when the device is supposed to be off. It is evaluated by the ratio of the high level  $U_h$  to the low level  $U_l$  of the signal. Figure 2.7 shows signals taken for both crystals using the same setup as before. In order to correctly evaluate both levels, it is necessary to note, that photodiodes are susceptible to dark noise, which is electrical noise falsely registered as light. To compensate for this, a dark image was taken, with the laser beam off, and the mean of the dark image was subtracted from the signals used to evaluate the extinction ra-

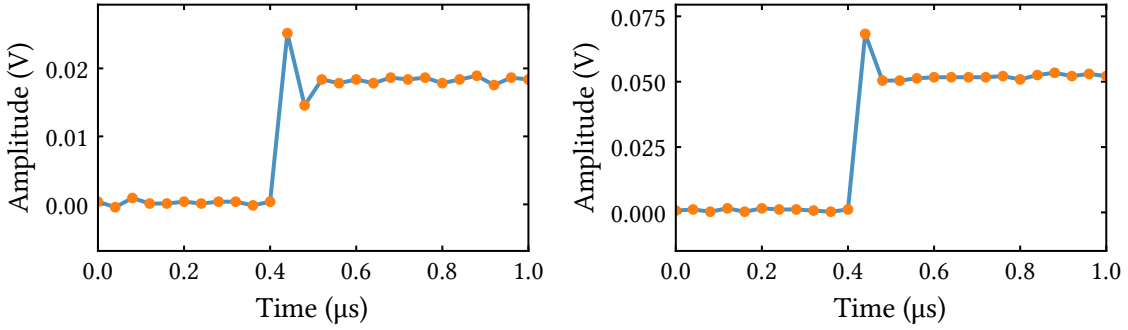


Figure 2.6.: The EOM was turned on, in order to measure rise times. However, the photo-diode and oscilloscope both limit the measurement with their bandwidth and sampling rate. However, an approximation to the rise time can be given, by subtracting the last data point on the low level and the first level on the high level, giving at least a fraction of a microsecond for both EOM types.

	$U_h$	$U_l$	$U_h/U_l$
RTP	$(1.90 \pm 0.06) \times 10^{-2}$	$(3.7 \pm 5.2) \times 10^{-4}$	$51_{-21}^{+\infty}$
BBO	$(5.46 \pm 0.08) \times 10^{-2}$	$(9.6 \pm 7.4) \times 10^{-4}$	$57_{-32}^{+247}$

Table 2.2.: Measuring the extinction ratio requires finding the high and low levels and calculating their ratio. It is noteworthy, that the standard error on the low level is of the order of the mean, therefore the ratio has an infinitely high upper bound.

tio. The high and low levels are then given by selecting points of the respective level after it has stabilized, which are highlighted in Figure 2.7. Giving an upper bound to the extinction proves difficult, as already the standard deviation on the low level for both crystals is on the order of the mean. In retrospect, the measurement can be improved by reducing the standard deviation on the levels, which should be possible by taking more signals and averaging them. Nonetheless, relevant parameters for the extinction ratio for both crystals are given in Table 2.2.

The manufacturer provides an extinction ratio for the RTP crystal of  $> 200 : 1$ , however no value is given for BBO. Therefore, the value provided by the manufacturer can certainly be verified with an improved measurement.

As the chopping frequency in the current experiment is limited to 1.4 MHz, the upper bounds for the repetition rate are also a crucial criterion that needs to be evaluated. The measurement showed for high repetition rates a resonance-like behaviour, where the am-

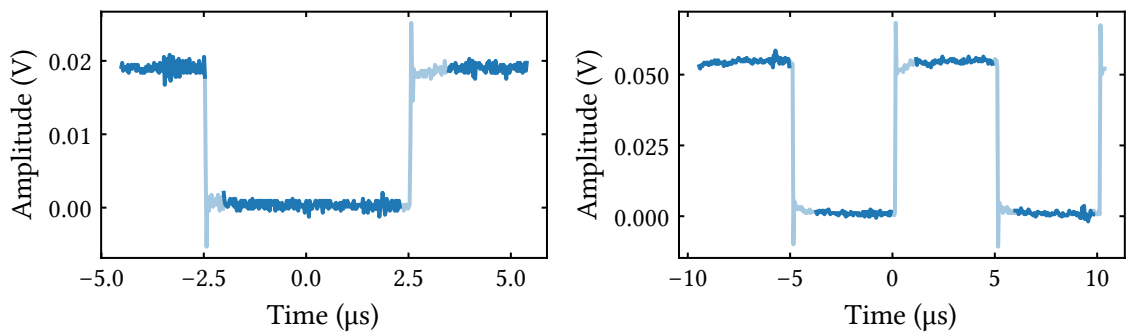


Figure 2.7.: Measurements of extinction ratio for RTP (left) and BBO (right). The highlighted values were used to find the high and low level, by taking their mean. However the uncertainty on the low level is too high to give a fair value on the extinction ratio.

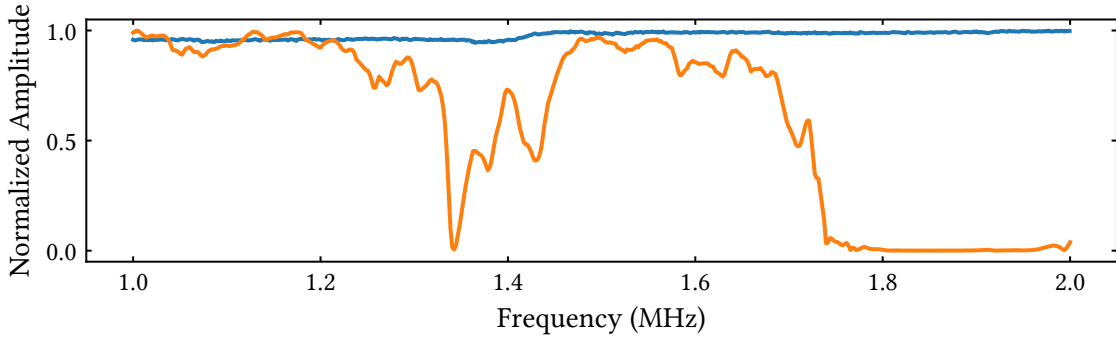


Figure 2.8.: Shown is the amplitude of a laser whose polarization was rotated by a Pockels cell and then filtered using a polarizing beam splitter. The frequency is the repetition rate of the voltage placed into the EOM. The two materials are RTP (orange) BBO (blue). The curves are normalized to their maximum value.

plitude of the signal from the Pockels cell was higher for certain repetition rates. This was most notable in the RTP crystal. To quantize this in more detail, the repetition rate was ramped up in 60 s intervals, after which the resulting signal was recorded and the amplitude evaluated. This results in the diagram shown in Figure 2.8. Measuring the signals showed, that this behaviour was worse if only one type of voltage was applied, therefore the choice of applying alternating voltages was made. The diagram clearly shows resonant-like behaviour for RTP. This means, that in the future, the chopping will have to be carried out around 1.5 MHz, where the amplitude of the signal is close to the maximum and therefore loss of laser power is mostly only insertion loss into the EOM.

## 3. Sorting of atoms

Tweezer arrays are especially suitable to study manybody systems, as arbitrary patterns can be configured, which is not possible when using optical lattices. In our experiment, atoms are cooled in optical molasses and loaded into tweezers in a chopping sequence, discussed in Chapter 2. However, in the loading stage, parity projection induces light assisted collisions of the atoms [24], which effectively heat pairs of atoms out of the trap. This leaves only sites occupied, that originally had odd number of atoms, resulting in a total occupation of 50% of atoms across the tweezer array. It is desired to have a fully occupied grid of atoms each run, however post-selection is unfeasible, as even on a  $3 \times 3$  grid of atoms, the chance of fully occupying the array is only  $0.5^9 = 0.2\%$ .

Consequently, the solution is to rearrange the atoms in the system, which has demonstrated before [8–10, 25]. As mentioned, the tweezers in our experiment are generated by SLMs. In order to rearrange the atoms however, they need to be transferred from the static SLM tweezers, into new dynamic acousto-optically deflected tweezers. These move the atoms adiabatically to new positions, while keeping the others stationary. In this way, atoms are moved along pre-calculated paths to fill gaps of the pattern. The following chapter discusses the sorting of atoms by using acousto-optical deflectors (AODs) as the device of choice for programmatically deflecting a laser beam. Using this device, it is also possible to generate an array of tweezers, so that multiple sites at the same time can be moved.

### 3.1. Acousto-optically deflected tweezers

Being able to quickly change the position of a laser beam is the most fundamental prerequisite of sorting atoms. The process has to happen on short timescales compared to the lifetime of atoms and with high accuracy. As AODs can fulfill this requirement, the process of light deflecting off a sound modulated crystal is discussed in the following. By applying sound waves, it is possible to move a laser beam or split it into multiple beams. The optical element handling the deflection is called an AOD and works very similar to an AOM.

However, in an AOD, the first deflected order is stronger and higher orders are generally not visible.

After going through the theory of acousto-optical deflection, the AODs in question are described, following the setup of generating the tweezers needed for the rearrangement of the atoms.

### 3.1.1. Acousto-optical effect

The acousto-optical effect describes the way optical waves deflect off sound waves in a solid medium, which is generally a crystal. This means, sound waves propagating the crystal modulate the positions of the atoms in the lattice, which in turn affects the refractive index on a macroscopic scale. If the sound wave is a planar wave, then the modulated refractive index is written as a function of position  $x$  and time  $t$  [22]:

$$n(x, t) = n - \Delta n_0 \cos(\Omega t - qx). \quad (3.1)$$

In this case, the offset  $n$  is the refractive index in absence of sound waves. Moreover,  $\Delta n_0$ , is the amplitude,  $\Omega$  the frequency and  $q$  the wavenumber given by the sound wave.

Using this relation, the next step is calculating the deflection angle off the medium. In the following, a short summary is given, the detailed analysis can be found in [22]. Starting from the assumption that the incident optical wave has a much higher frequency than the sound wave, then the light entering the medium sees the sound waves as stationary and the medium's crystalline shape is given by the sound wave.

Then the description of light passing through a medium is given by the Bragg condition, and is used to calculate how light is partially reflected when leaving the medium. In order to calculate this quantity, the medium is broken up into slices, off which the optical wave partly reflects, given by the Bragg diffraction. Each slice has a partial reflectance amplitude  $\Delta r$ , depending on the refractive index  $n$  and the angle of the incident optical beam with respect to the medium. The total reflectance amplitude  $r$  can then be calculated by integrating over all slices and carries over the dependence on the angle. By maximizing this relation, the angle resulting in the maximum reflectance amplitude is given by the Bragg condition:

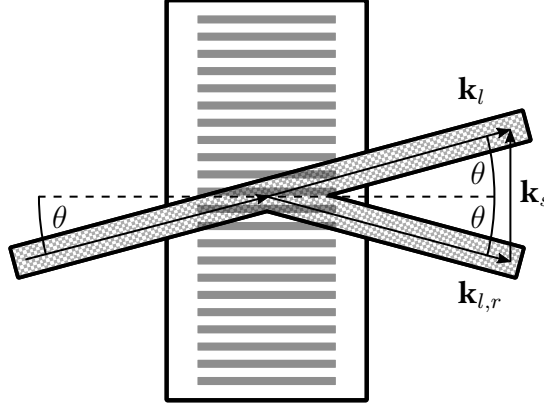


Figure 3.1.: Schematic operation of an AOD. Light waves travelling in direction  $\mathbf{k}_l$  are deflected off the sound waves with direction  $\mathbf{k}_s$ , resulting in a reflected beam  $\mathbf{k}_{l,r}$ . The optical waves are deflected under the Bragg condition, which can be calculated via the momentum conservation  $\mathbf{k}_{l,r} = \mathbf{k}_l + \mathbf{k}_s$ .

$$\sin \theta = \frac{\lambda_l}{2\lambda_s}, \quad (3.2)$$

where  $\lambda_l$  and  $\lambda_s$  refer to the wavelength of the light and sound waves respectively.

The maximum of the reflectance amplitude with respect to the angle is very sharp, such that there is a deflected beam only if the angle between the wave vectors of the optical wave  $\mathbf{k}_l$  and the sound wave  $\mathbf{k}_s$  matches the Bragg condition. Thus, from momentum conservation in Figure 3.1, one arrives at the same condition:

$$|\mathbf{k}_l| = |\mathbf{k}_{l,r}| = \frac{2\pi}{\lambda_l} \quad (3.3)$$

$$|\mathbf{k}_s| = \frac{2\pi}{\lambda_s}, \quad (3.4)$$

it follows directly, that

$$\sin \theta = \frac{|\mathbf{k}_s|/2}{|\mathbf{k}_{l,r}|} = \frac{\lambda_l}{2\lambda_s}. \quad (3.5)$$

Using the acousto-optical effect in order to modify tweezer positions, it is necessary to break the dependence of the angle between incoming optical wave and acoustic wave, while keeping the dependence on the angle of the outgoing light. This is achieved by modelling

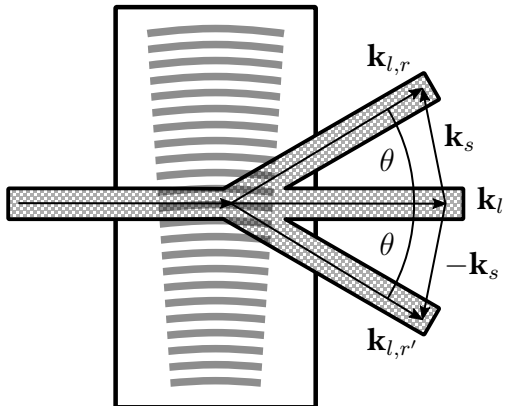


Figure 3.2.: Similar to Figure 3.1, light is deflected off sound waves in an acousto-optical medium. This time, the sound wave is modelled as a radial wave, such that besides the transmitted component, two more orders are deflected.

the sound wave as a radial wave, travelling outwards from the origin of the sound. As a consequence of this, within a certain bandwidth, it will always be possible to fulfill the Bragg condition, no matter how the light enters the medium.

In Figure 3.2, an optical beam enters a medium straight and exits on a diffracted angle  $\pm\theta$ , given by the Bragg condition. Using again the momentum conservation from Equation 3.5, there are now additional acoustic waves travelling in opposing directions, where the optical and sound wave meet. In the approximation of small angles, the Bragg condition then simplifies to:

$$\theta_{\pm} \approx \sin \theta_{\pm} = \pm \frac{|\mathbf{k}_s|}{|\mathbf{k}_l|} = \pm \frac{\lambda_l}{\lambda_s} = \pm \frac{f_s}{v} \lambda_l, \quad (3.6)$$

where the speed of light in the medium  $v$  needs to be taken into account.

This means, that the angle of the first deflected orders from the AOD only depend on the wavelengths of the light wave  $\lambda_l$  and the sound wave  $\lambda_s$ . In other terms, the angle of deflection can be tuned by changing the wavelength of the sound wave. As the deflector is driven with an RF-generator, we generally speak of the frequency and not the wavelength of the sound wave. Using the deflector for sorting, means taking first deflected order and blocking the others. This way, a beam can be moved by driving a frequency ramp on the sound wave, thus changing the angle of the first deflected order. Consequently, the change of angle depending on the change in frequency of the sound wave is interesting and is then calculated as:

$$\Delta\theta_{\pm} = \pm \frac{\Delta f_s}{v} \lambda_l \quad (3.7)$$

Thus, all parameters required for manipulating the position of laser beam have been calculated, such that the tweezers can be operated for resorting. We have seen how optical light is deflected off sound waves in media and how this can be used to re-position laser beams and in the long run, move atoms along paths. There are generally two types of AODs available, that are normal mode and shear mode. In a normal mode AOM, the shape of the crystal viewed from the top, is rectangular, while in a shear mode, the crystal's front and back sides are cut at an angle. This means, sound waves won't be radial anymore, but instead be shear waves, meaning their velocity is slower. This is in general preferable, as we made the assumption, that the speed of the sound wave is much slower than the speed of the light wave, and thus this condition is reinforced. All in all, after having understood the operation of AODs, the following chapter explains the setup in place for sorting the atoms.

### 3.1.2. Preparation of the tweezers beams

With the derivations from the previous chapter, it is possible to calculate the position of the laser beam, depending on the frequency of the sound wave propagating the AOD. However, the beam has to be prepared before entering the deflector, meaning its polarization has to be adjusted. After the deflector, the beam will pass an objective into the vacuum chamber and therefore needs to be shaped correctly before the objective. The setup of the laser, as well as the configuration of AODs, in order to sort in two dimensions, is described in the following.

The deflectors ((AA DTSXY-400-800.860) from Pegasus optics) and their characteristics are given in Table 3.1.2. The AODs are driven by RF-frequencies, which map 1:1 to the frequency of the sound wave. In order to deflect in two dimensions, two deflectors are placed in series, which are turned by  $90^\circ$  with respect to each other. This way, the first order on the first AOD will extend e.g. into the x-axis, while the first order of the second AOD will then extend along the y-axis. Together, exiting the deflectors will be a  $2 \times 2$  grid of laser beams, which can be seen in Figure 3.3. These are the  $(x = 0, y = 0)$ ,  $(1, 0)$ ,  $(0, 1)$  and  $(1, 1)$  orders, however, only the  $(1, 1)$  order will be used, as this is the one that is deflected based on the sound wave placed into the AOD.

Central drive frequency at 795 nm	$(102 \pm 4)$ MHz
Bandwidth	36 MHz
Max optical power density	$5 \text{ W mm}^{-2}$
Max RF power	2 W
Laser beam diameter [ $D$ ]	$500 \mu\text{m} < D < 6 \text{ mm}$
Material (speed of sound)	TeO <sub>2</sub> ( $650 \text{ m s}^{-1}$ )
Scan angle	$(44 \text{ mrad})^2$

Table 3.1.: Properties of AA DTSXY-400–800.860 crossed AODs from Pegasus optics.

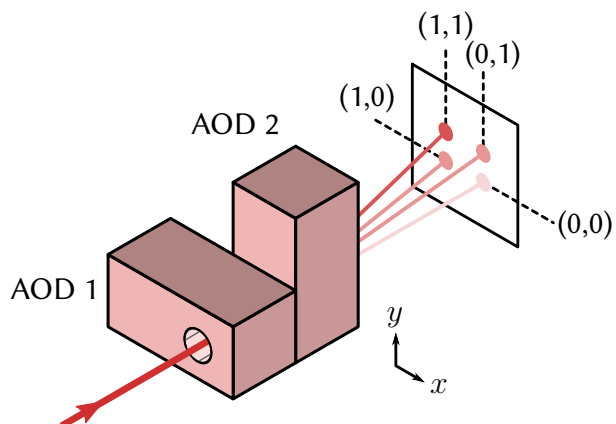


Figure 3.3.: Light passing through two AODs is deflected into a 2-dimensional grid. The colors refer to the optimized power going into the respective order, from lightest color being lowest power to darkest color being highest power. This way, the least amount of power goes into the (0,0) order and most into the (1,1) order.

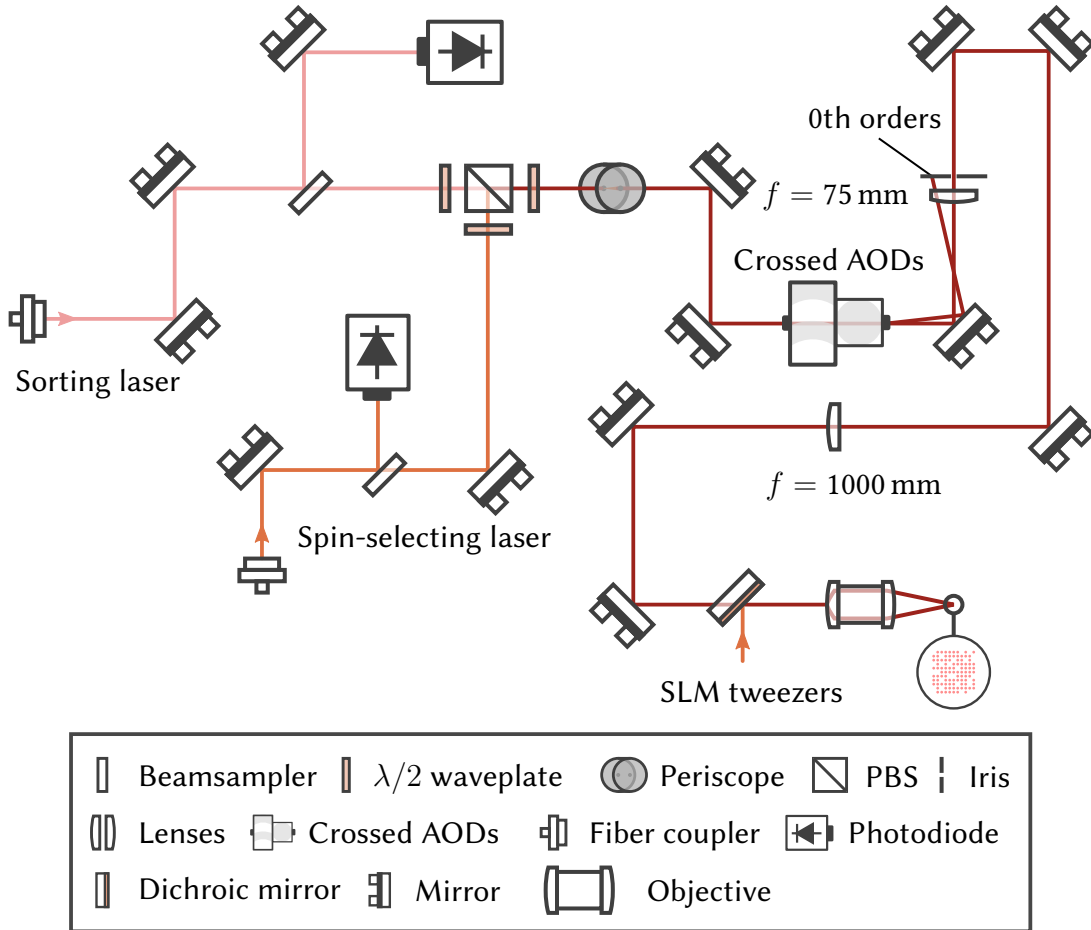


Figure 3.4.: Beam path to generate acousto-optically deflected tweezers. Two beams used for sorting and spin-resolved imaging are combined using a PBS. They pass the AOD after which the beam is shaped to match the objective into the experimental chamber.

The details of the configuration and characterization of the devices used in the experiment are given in [19]. The crossed AODs configuration described above is used in the following for rearranging the atoms. Additionally, the dynamic tweezers generated from the deflectors are also used for a spin-selective imaging approach, which is further described in Chapter 4. This means, beam paths of two different lasers are passing through the same deflectors. In Figure 3.4, the setup including both laser beams is shown. The first laser, used for the characterization in [19] and later sorting of atoms, as well as for testing reasons regarding the tweezers in the following and has a wavelength of 795 nm. The spin-selective laser has a wavelength of 768 nm and is further discussed in Chapter 4.

The first step in the setup, is stabilizing the intensity of laser beams, by measuring their power on a photodiode and using proportional-integral controllers to adjust the signal. They then pass a  $\lambda/2$  waveplate to adjust the polarization, which affects the efficiency of

the AOD. The deflectors, which are connected to RF-synthesizers, then produce the  $2 \times 2$  grid of laser beams. Afterwards, a  $f = 75$  mm lens, projecting the center of the AOD-array, extends the beam spatially until it is collimated using a  $f = 1000$  mm lens. This sets the correct beam size for the objective to project the beam onto the atoms.

### 3.1.3. Moving tweezers

It was shown, how the position of the laser is calculated using the Bragg condition in Equation 3.1.1. With the laser setup in place, the question remains how the change of the sound wave frequency affects the position of the tweezer in the plane of the atoms, where the AODs are in the Fourier plane. This is calculated, by taking into account the magnification  $M$  due to the telescope created between the  $f = 1000$  mm lens and the objective, having an effective focal length of 33.18 mm. From the point of view of the atoms, this results in  $M = \frac{1000}{33.18} = 30.14$ , meaning the distance between the atoms  $\Delta x$  is magnified by this amount. Continuing from the atom's reference frame, their magnified distance is then given on the  $f = 75$  mm lens as a distance  $\Delta x_{magnified} = Mx$ , which projects the position into the center of the crossed AOD configuration at an angle  $\tan \theta \approx \theta = \Delta x_{magnified}/75$  mm. With Equation 3.1.1, this results in a change of frequency on the AOD:

$$\Delta f = \frac{\Delta x_{magnified} v}{75 \text{ mm}} \frac{v}{\lambda}, \quad (3.8)$$

given an optical laser wavelength of  $\lambda$ . The speed of sound for the AODs, which is the speed of sound in  $\text{TeO}_2$  is  $v = 650 \text{ m s}^{-1}$ . This means a typical atomic distance of  $10 \mu\text{m}$ , requires a change in frequency of  $\Delta f = 330 \text{ kHz}$ .

### 3.1.4. Tweezer homogeneity

With all the building blocks in place for driving acousto-optically deflected tweezers, they are now ready to be imaged and tested. The beam path shown in Figure 3.4 was used, except the objective at the very end was replaced by a  $f = 500$  mm lens and a camera (XIMEA MD028MU-SY). This way, the tweezers are visible directly on the camera. Moreover, in order to measure the homogeneity more accurately, part of the beam is split and coupled into a photodiode after the  $f = 500$  mm lens. This way, an image was taken with a camera and at the same time, a trace was taken from the signal of the photodiode. Although it is

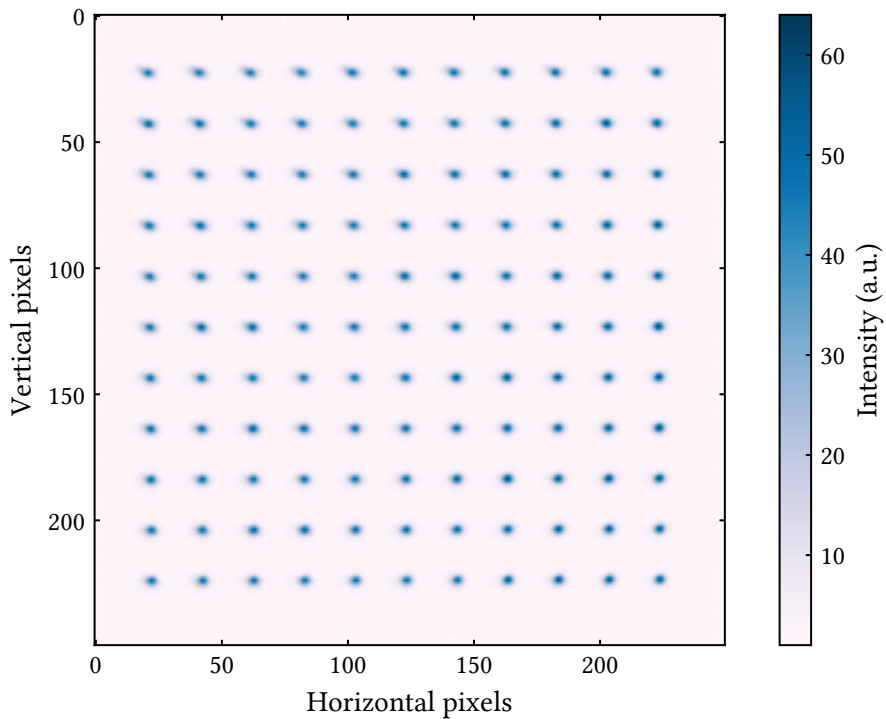


Figure 3.5.: An image of tweezers was acquired by activating a set of  $11 \times 11$  frequency combinations on the crossed AODs. A slight field of view effect is visible in the top-left corner.

technically possible, to draw a grid with the AODs, by applying a superposition of multiple frequencies, the measurement discussed in the following was taken by turning on each tweezer separately one after another. This way, they can be distinguished powerwise.

The Figures 3.5 and 3.6 show the results of these measurements. It can be seen in the camera image, that there is a slight field of view effect in the top-left corner. From the photodiode trace, the homogeneity can be evaluated more clearly and is shown as a histogram and a heatmap, confirming the field of view effect. This shows, that the intensity difference between the first and last set of tweezers is about 10% when the distance between lattice points was given by a frequency difference 1 MHz. This, however, is when only one tweezer is running at the same time. In the case of multiple tweezers, interference between the acoustic waves will most likely not result in the same results and will give much less homogeneity.

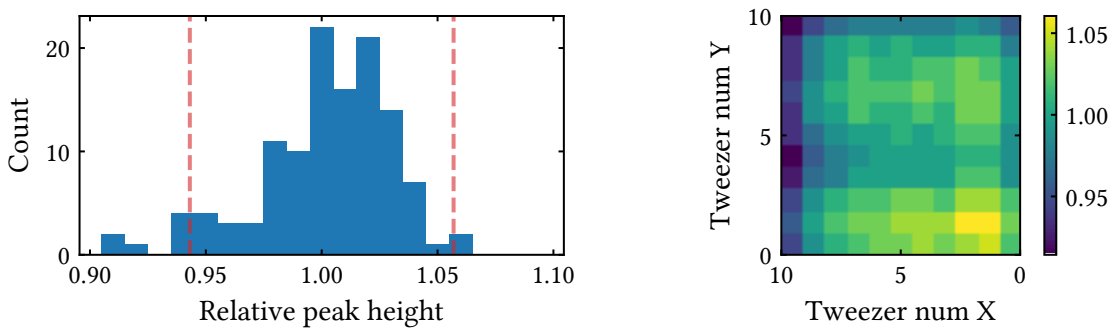


Figure 3.6.: The same tweezer picture as in Figure 3.5 was acquired using a photodiode. The homogeneity is then evaluated by counting the peak heights in the form of a histogram. The distribution is almost Gaussian, therefore one standard deviation is shown as dashed red lines. The difference between maximum and minimum peak height is around 10%. Shown to the right is a heatmap of the same tweezer homogeneity and a clear trend is visible, where the tweezers in the lower right corner have most power.

### 3.2. Sorting algorithms

With the laser now passing through the crossed AODs and being shaped for the objective, it is time to rearrange the atoms for the experiment. Doing so requires the knowledge about unloaded SLM tweezers, which is achieved by imaging the atoms and evaluating their positions. Of course, atoms can't be lost during imaging, therefore cooling and trapping beams are chopped together and the scattered light from the cooling beam is recorded as a fluorescence image. From then on, atoms need to be moved along paths in order to fill the vacancies. They can be lost, if the move is on the order of the scattering rate, as then the trap moves out of range while an atom is in the excited state. Generally speaking, the move needs to be as fast as possible, since heating effects lead to  $1/e$  lifetimes on the order of 80 seconds in our experiment. Therefore, already 1.2% of atoms, or at least one atom in a  $10 \times 10$  grid are lost after one second.

Sorting the atoms as fast as possible in order to reach 100% filling requires paths that minimize the total sorting time. An obvious choice here is Dijkstra's algorithm, which is designed to find the minimal path between two points in an arbitrary landscape. However, since the paths have to be calculated while the atoms are loaded, this means computation complexity has to be taken into account as well. Since Dijkstra's algorithm scales at best with  $\mathcal{O}(n^2 + n^2 \log(n^2))$ [26], where  $n$  is the number of atoms, this can lead to long computation times. However, some simplifications can be made, which can help come up with an algorithm that is both fast in calculation speed, as well as having fast sorting speeds.

For one, we are operating on a rectangular grid and thus make the simplification to only move vertically or horizontally and not diagonally. Secondly, atoms that have started moving, stay in the tweezer until they arrive at their destination, and thus the tweezer does not suddenly jump to a new target. This is a sensible simplification, as an atom has to be transferred from the initial tweezer array to the moving tweezers (and back again when it arrives at the destination), which also takes up time. In the description of the algorithms, the grid is separated into a target and a reservoir region. This means we are trying to get a 100% filling in the target region, by moving atoms out of the reservoir region. Any atoms left in the reservoir after the sorting is finished, will be discarded. On the other hand, while there are still holes in the target region, the algorithm will look for ways to fill the gaps using atoms from the reservoir region.

Two algorithms (pathfinding and compression) are presented in the following, one is based on solving a pathfinding problem and moves one atom at a time. The other uses the feature of the AOD and its driver (discussed later), that allows to work move several tweezers at once, by applying multiple RF frequencies, in order find a more parallelized approach.

### **3.2.1. Pathfinding**

The pathfinding problem is solving the problem of finding the shortest path between two points. For sorting of atoms, this means identifying the shortest set of movements to relocate an atom from the reservoir region to an empty spot in the target region. The algorithm described in the following was developed by Jan Werkmann<sup>1</sup> and is discussed in [27]. With the simplifications of above, atoms only move either horizontally or vertically. The algorithm will then identify a path that first moves the full distance of the one dimension, then the full distance in the other, at which point the atom has arrived at its destination. This is a sensible approach, as only one frequency ramp per dimension is driven, but does not change the total distance moved, since the atom won't move on diagonals. Then there are only two possible paths every atom can take, either going first vertically then horizontally, or the other way around. The optimal path is then the one with the least amount of atoms in it. If there happens to be an atom in the path, the algorithm segmentizes the path, moving the obstacle atom along the path into the unoccupied spot, with the other atom following after. An example path is shown in Figure 3.7. This then means, that by using the third dimension and moving the atom around the obstacles would improve the algorithm, as obstacle atoms can stay in place. In this experiment, this could be achieved by using a tunable lens.

---

<sup>1</sup><https://github.com/PhyNerd/GridRouting>

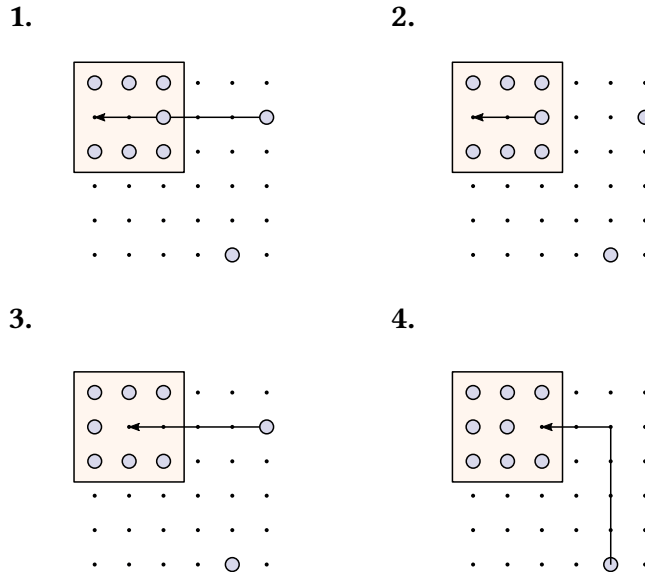


Figure 3.7.: Conceptual illustration of the pathfinding algorithm for resorting. The atom tries to move into a hole but has an obstacle (which is just another atom) in its way. The obstacle is first moved out of the way, after which the atom follows. The target area is then further filled with the remaining atom.

### 3.2.2. Compression

As was just discussed, the pathfinding algorithm moves atoms one by one. However, one might want to find a way to parallelize sorting, therefore decreasing the sorting time. By supplying an AOD with multiple RF-frequencies, it is possible to create multiple movable tweezers. The compression algorithm discussed here makes use of this in order to reduce the total time of the sorting, as well as having a lower computation time with respect to the pathfinding algorithm.

The compression algorithm works by picking a full line of atoms. It then moves the selected atoms along the line towards the target area, grid point by grid point. If an atom would collide with an obstacle, that is, either another atom not currently inside an AOD tweezer, or the end of the target area, then that atom is transferred back to the SLM tweezer grid, and not moved in the next step. This process is shown in Figure 3.8. When one line is finished moving according to this end condition, the next line is picked up and the process repeated. This is done first for all rows, then for all columns, and finally, all atoms are found in one corner of the grid. Doing it this way, effectively compresses all atoms in the grid into an area.

Due to the nature of the algorithm, there can still be holes in the target area when the sequence is finished. To overcome this problem, following the compression stage, the

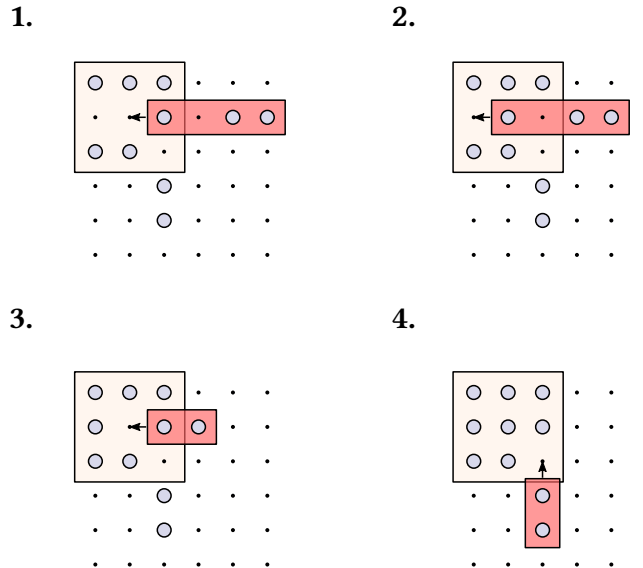


Figure 3.8.: Sorting atoms using the compression algorithm is done by selecting a full line of atoms. They are then moved towards the left edge. An atom that meets the edge is released before the others continue moving. When the steps for the rows have been completed, the same process follows for the columns.

pathfinding algorithm will fill the final few gaps, whose runtime is favorable towards low vacancy numbers.

To further take advantage of the compression algorithm, a geometry is chosen, which has the target area in the center of the grid and the reservoir surrounding it, as seen in Figure 3.8. As the algorithm pushes the atoms into a corner, the grid can simply be split up into four sections. Then the moves for each section are individually calculated. Ending up with moves in the row-dimension and moves in the column-dimension for each section, they can then be merged together, if they operate on the same line, which is illustrated in Figure 3.9. As such, the sorting time of moving atoms into one corner is effectively the same as moving the atoms into the central area, by splitting it up into sections and merging the steps.

### 3.2.3. Comparison of the two algorithms

As the pathfinding and compression algorithm are both solving the same sorting problem, it is necessary to make a performance comparison between the two. For the simulation of the performance comparison, the target area was chosen to be in the center, surrounded by the reservoir region. This gives a geometry, which has holes as close as possible to reservoir atoms, therefore giving a minimal number of movements for the pathfinding algorithm, while also making use of the performance gain that was highlighted in Section 3.2.2 for the compression.

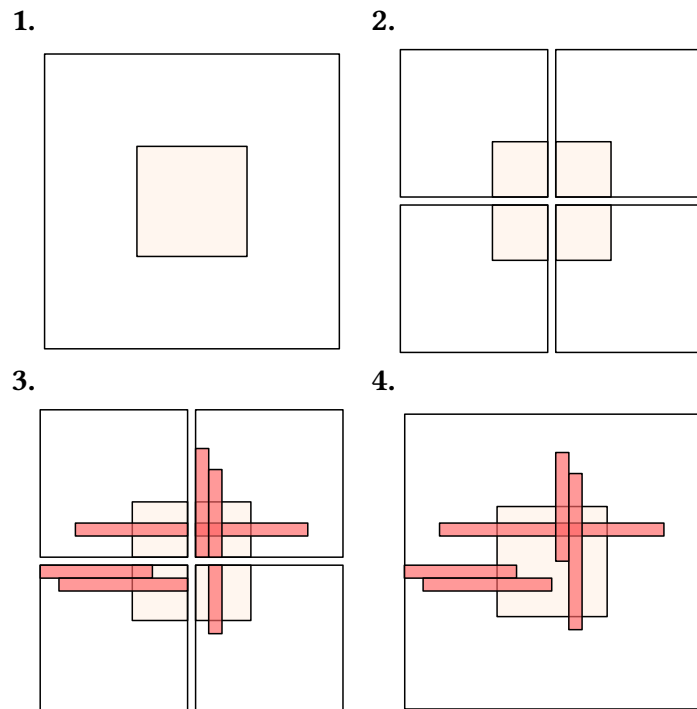


Figure 3.9.: Sequence of finding parallelized paths for the compression algorithm. Since atoms are always sorted into a corner, the compression algorithm can be split into four sections. Therefore from 1. to 2., the region of interest is split into four sections. In 3., paths are calculated for each section individually and are then merged (and therefore parallelized) in 4., when they are acting on the same row (or column).

Relevant parameters that need to be compared, are the sorting and computation time, as they need to be much slower than the lifetime of the atoms. Atom loss can also occur, whenever the atoms are transferred from the SLM tweezer grid to the AOD tweezer grid used for the sorting. This way, the number of transfers are also shown in the following. Simulations were performed, by populating the full grid with atoms with 50 % probability of occupying a grid point. Then each algorithm was run and relevant parameters recorded. Simulations were run for various grid sizes, while trying to keep the fraction of number of atoms in the target area  $N_{target}$  to the number of atoms in the reservoir area  $N_{reservoir}$  around  $\frac{N_{target}}{N_{reservoir}} \approx 0.65$ . This has to be compromised for low grid sizes, as the integer nature of grid points only allows natural numbers for reservoir sizes.

The results in Figure 3.10 show that the compression algorithm has a faster sorting and computation time, but has to transfer more atoms into the AOD tweezer grid. However, it also shows that it scales better for increasing grid sizes. A polynomial fit is shown for the second half of the points, where the rounding issue is less present. The fit parameters are given in Table 3.2.3, from where it can be seen, that the compression algorithm scales more linearly than the pathfinding algorithm.

### **3.3. Driving an RF-synthesizer for arbitrary pattern generation**

One of the most powerful aspects about AODs is the fact, that a superposition of sound waves results in a superposition of light waves in the output. This way, it is possible to generate a grid of tweezers, by supplying each AOD with one or more RF-frequencies. There are a multitude of ways to generate RF-frequencies, one way is using voltage controlled oscillators (VCOs), which can be simple LC-circuits. Using these, it is also possible to drive frequency ramps, however it is not possible to synthesize multiple frequencies from one VCO, meaning it is necessary to use multiple VCOs together. Therefore using this approach it is possible to sort the atoms one-by-one, however it is not possible to generate grid patterns.

To overcome this issue, we implement a digitizer card (M4i.6600-x8, Spectrum Instrumentation), whose specifications are summarized in Table 3.3.1. Doing so allows to sample arbitrary signals, for example sines, rectangles or even non-periodic ones. A digital-to-analog converter (DAC) on the board converts the sampled points into an analog signal, which can be passed into the AOD.

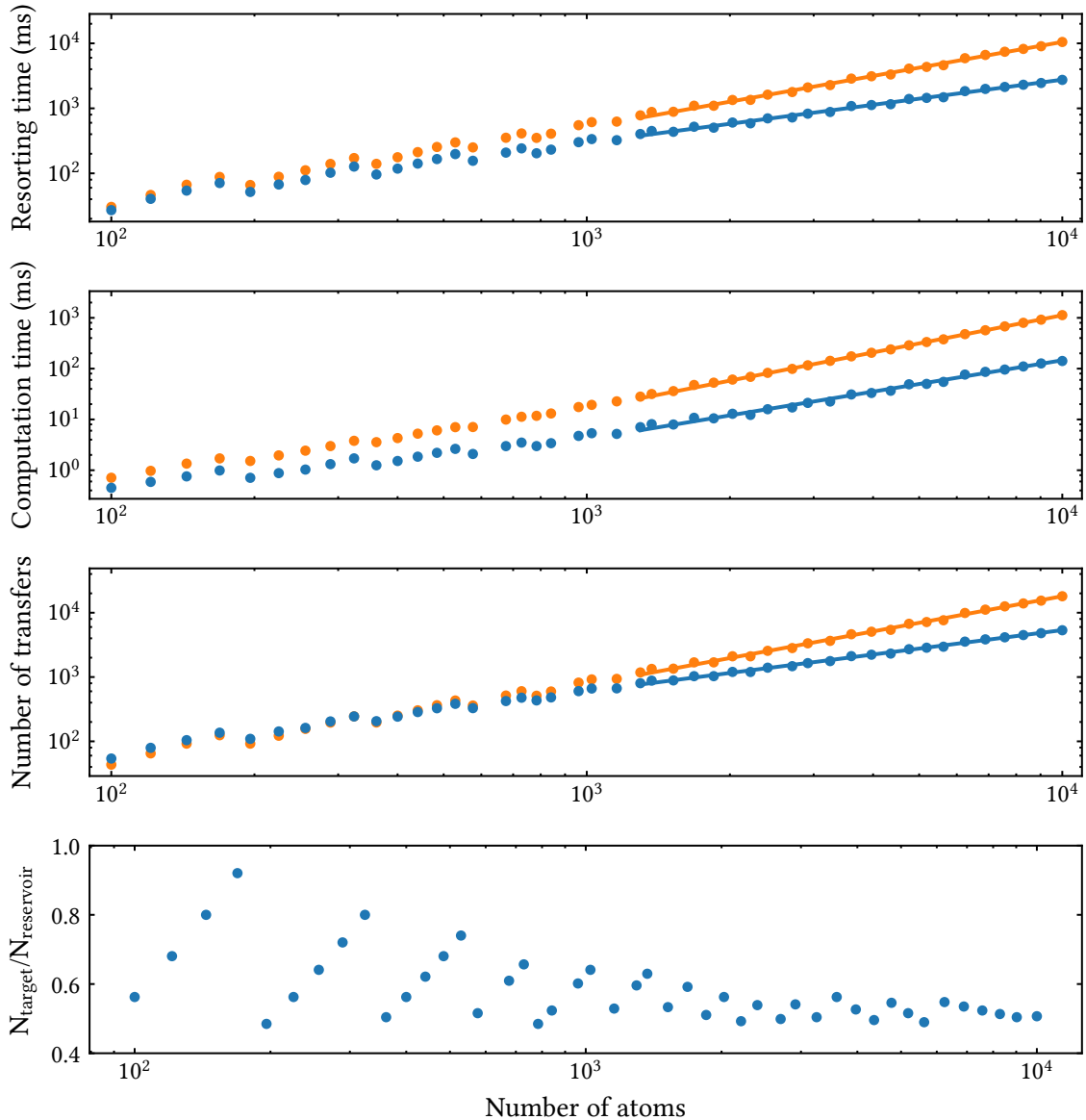


Figure 3.10.: Comparison of pathfinding algorithm (orange) and compression algorithm (blue) for sorting atoms into a target region. For each data point, 50 simulations were run and the mean of the result is shown. Standard deviation is on the size of the dots drawn and as such are not visible. The fraction of atoms in the target versus the reservoir area are shown in the last diagram. Since only integer values are allowed for the reservoir size, the fraction between the two sees a rounding effect. For this reason, the fit is only done for the upper half of the data points, where the effect is less pronounced. The values to the fit are given in Table 3.2.3.

Pathfinding		
	$m$	$a \text{ (ms)}$
Resorting time	$1.3 \pm 1.7 \times 10^{-2}$	$5.8 \times 10^{-2} \pm 8.8 \times 10^{-3}$
Computation time	$1.8 \pm 8.9 \times 10^{-3}$	$4.8 \times 10^{-5} \pm 3.8 \times 10^{-6}$
Number of transfers	$1.4 \pm 1.8 \times 10^{-2}$	$5.7 \times 10^{-2} \pm 9.2 \times 10^{-3}$

Compression		
	$m$	$a \text{ (ms)}$
Resorting time	$9.7 \times 10^{-1} \pm 1.7 \times 10^{-2}$	$3.6 \times 10^{-1} \pm 5.3 \times 10^{-2}$
Computation time	$1.6 \pm 3.1 \times 10^{-2}$	$9.0 \times 10^{-5} \pm 2.5 \times 10^{-5}$
Number of transfers	$9.5 \times 10^{-1} \pm 1.2 \times 10^{-2}$	$8.3 \times 10^{-1} \pm 8.6 \times 10^{-2}$

Table 3.2.: Comparison of scaling of the two sorting algorithms. For each quantity given in the left-most column, a polynomial  $f(x) = aN^m$  was fitted to the points shown in Figure 3.10. This gives  $m$  as the scaling and the parameter of interest, resulting in better scaling in every aspect for the compression algorithm.

Maximum sampling rate	$1.25 \text{ GS s}^{-1}$
Output level (at max sampling rate)	$\pm 4 \text{ V}$
Transfer speed PC to card	$2.8 \text{ GB s}^{-1}$
Memory	4 GB

Table 3.3.: Relevant parameters of the Spectrum M4i.6600-x8 card from the specifications given by the manufacturer.

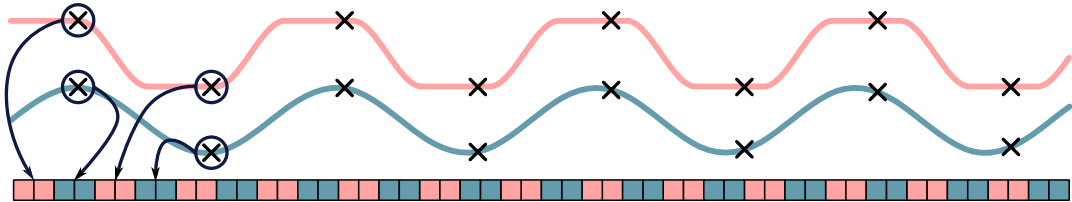


Figure 3.11.: Sampled data points are stored in a local buffer, which can then be transferred into the cards memory. The memory is effectively 1-dimensional, with two bytes for each sampled data point. Example signals are given for Channel 1 (red) and Channel 2 (blue). In the single replay mode, the data pointer will read from the first memory position until a given end point. In sequence replay mode, the data pointer will move forward, but can jump at any point based on user preference.

### 3.3.1. Functionality of the Spectrum driver

Communication with the card is provided through a low-level interface from the official drivers over a PCIe slot. In the following, two replay modes of the spectrum card are discussed, which are standard replay mode and sequence replay mode. In single replay mode, a signal is sent onto the card, which is played back a set number of times, from start to finish. The sequence replay mode allows to upload sequences during initialization. It is then possible to play any arbitrary combination of the sequences one after another.

The functionality of the card depends on two factors: The layout of the memory, and the readout speed (the sampling rate) of the memory. In the following implementation, two output channels of the spectrum card are used. Doing so, the memory is formatted, such that two bytes of channel 1 data are followed by two bytes of channel 2 data as seen in Figure 3.11. Transferring data onto the memory then requires to fill a buffer, that is, memory on the computer running the driver, that has the same layout as the spectrum card's memory.

With this information, the structure of a program driving the digitizer card follows the format given in Table 3.3.1.

Single replay mode	
Initialization phase	<ul style="list-style-type: none"> <li>• Set sampling rate</li> <li>• Set replay mode to single replay mode</li> <li>• Allocate the buffer memory</li> </ul>
Main loop	<ul style="list-style-type: none"> <li>• Sample datapoints of the signal to play and move into the buffer</li> <li>• Transfer datapoints from the buffer to the card</li> <li>• Replay signal <math>N</math> times</li> </ul>
Sequence replay mode	
Initialization phase	<ul style="list-style-type: none"> <li>• Set sampling rate</li> <li>• Set replay mode to sequence replay mode</li> <li>• Sample signals to use in the sequence programmed later</li> <li>• Transfer signals onto the card</li> <li>• Allocate the buffer memory (will contain information about the sequence)</li> </ul>
Main loop	<ul style="list-style-type: none"> <li>• Fill buffer with information about which signals to play</li> <li>• Transfer buffer to the card</li> <li>• Play sequence</li> </ul>

Table 3.4.: Difference in programming when using either the single replay or the sequence replay mode of the Spectrum M4i card. In this case, it is instructive to see, that the single replay mode has an overhead during the main loop compared to the sequence replay mode, which has all sequences stored in memory already.

The maximum transfer speed for transferring data from the PC to the spectrum card is limited by the hardware to  $2.8 \text{ GB s}^{-1}$ . This means that it will always be preferable to move as few data as possible. Consequently, if possible, it is advantageous to use the sequence replay mode, as here, almost all data is already transferred in the initialization phase. All that is left to transfer, is the sequence the data pointer is following.

### 3.3.2. Limits of using the card in the experiment

There are some considerations to make when using a digitizer card as a driver for acousto-optical tweezers. Since the digitizer replays sampled data points from waveforms, this means data points need to be transferred from a computer memory to the digitizer card. The transfer time should of course be kept minimal, since the information about which waveforms to sample is only available when atoms are already loaded into tweezers and their lifetime in the tweezer traps is finite (on the order of 80 s for our experiment). Transferring data points to the spectrum card can be done in advance in the sequence replay mode, however this requires the internal memory of the digitizer to be big enough to hold all possible waveforms to be replayed. Both the transfer time and memory usage are calculated in the following, considering both the standard replay mode and the sequence replay mode.

In order to calculate the transfer time and memory usage, some assumptions need to be made. The assumptions and all necessary variables are summarized in Table 3.3.2. First of all, the central frequency of the AOD is approximately  $f_{AOD} = 100 \text{ MHz}$ . Therefore, in order to sample a sine at this frequency with at least 10 points per oscillation, means a sampling rate of at least  $1 \text{ GS s}^{-1}$  needs to be applied. For the M4i digitizer card, this means the next available setting is  $1.25 \text{ GS s}^{-1}$  and gives about 13 samples per oscillation. Being able to resolve the signal clearly, has the advantage to generate the frequency more accurately, therefore the 10 samples per oscillation is a good limit.

Now in order to calculate the time to transfer an atom adiabatically from the SLM tweezer grid into the AOD tweezer grid (and back again), the relation  $\dot{w} > w^2$  needs to be fulfilled, where  $w$  is the trap frequency in transverse direction. The following argumentation follows the directions in [28]. In our case, this is on the order of 20 kHz and is fulfilled for a transfer time of  $t_{transfer} = 1 \text{ ms}$ . To calculate the moving time  $t_{move}$  for an atom from one grid point to another, the shape of the trap is considered. If the atom is accelerated in the first half of the movement, and decelerated in the second half of the movement, the total distance to transfer the atom is given as  $L = at_{move}^2$ . The maximal acceleration is found from the trap waist  $w = 1 \mu\text{m}$  and its radial frequency  $f_{rad} = 100 \text{ kHz}$ , as  $a_{\max} \approx wf_{rad}^2 = 10^4 \text{ m s}^{-2}$ .

Variable	Used or assumed value
Sampling rate	1.25 GHz
Central AOD driving frequency	100 MHz
Adiabatic transfer time to new grid	1 ms
Adiabatic movement time to next grid point	1 ms
Grid size	$10 \times 10$
Number of tweezer transfers for sorting	60
Number of movements for sorting	40

Table 3.5.: Variables and assumptions used in the calculations for estimation of data transfer time and memory usage under the consideration of the experiment discussed in this thesis.

Therefore, choosing a conservative acceleration  $a = 10 \text{ m s}^{-2}$  results in a moving time  $t_{move} = 1 \text{ ms}$  over a distance  $L = 10 \mu\text{m}$ .

With the transfer time, moving time, and sampling rate in place, the size of one signal to move and transfer an atom, can be calculated as:

$$n_{points} = St = 1.25 \text{ GS s}^{-1} * 1 \text{ ms} = 1.25 \times 10^6 \quad (3.9)$$

$$M_{sig} = 2 \text{ B} * n_{points} = 2.5 \text{ MB}, \quad (3.10)$$

where 1 B is one byte and  $t = T_{move} = t_{transfer}$ . From the simulations of the algorithms in Figure 3.10, we see that assuming a  $10 \times 10$  grid, there are about 60 transfers from the SLM to the AOD grid (or the other way around) and 40 movements for one sorting. This means 100 sequences need to be played per channel, which is  $n_{seq} = 200$  in total. Lastly, the memory for all signals needs to be aligned to a power of two. Therefore, from the transfer speed  $v_{transfer}$  in Table 3.3.1 follows the time it takes for one transfer  $t_{transfer}$ :

$$t_{transfer} = \lceil n_{seq} M_{sig} \rceil_2 v_{transfer} = 183 \text{ ms}, \quad (3.11)$$

where the symbol  $\lceil \dots \rceil_2$  refers to rounding up to the next power of two. These calculations set the limit for the single replay mode, however, in the sequence replay mode, the limiting

factor is the memory it takes to store all possible sequences. The storage of the sequences already assumes knowledge of the composition of both channels. Therefore it is necessary to upload every relevant combination of signals for both channels. Working again with a  $10 \times 10$  grid of atoms, all relevant signals are found from the following table:

Signals on channel 1	Signals on channel 2	Usage
10 intensity ramps up	10 intensity ramps up	Transfer into AOD grid
10 intensity ramps down	10 intensity ramps down	Transfer out of AOD grid
9 frequency ramps up	10 constant frequencies	Move along x-axis
9 frequency ramps down	10 constant frequencies	Move along x-axis
10 constant frequencies	9 frequency ramps up	Move along y-axis
10 constant frequencies	9 frequency ramps down	Move along y-axis

Thus, by multiplying the signals in the columns and then adding the rows, there are 560 combinations and  $n_{seq} = 560 * 2 = 1120$  signals to upload onto the card. Each having a size of  $M_{sig} = 2.5$  MB results in a required memory of  $M_{req} = 2.8$  GB. More generally, on a NxM grid, the number of sequences can be calculated via

$$n_{seq} = 2NM + 2N(M - 1) + 2(N - 1)M \quad (3.12)$$

and therefore the required memory is

$$M_{req} = 5 \text{ MB} * n_{seq}. \quad (3.13)$$

With the calculations above, it is possible to apply the pathfinding sorting algorithm to the atoms in a timely manner. However for the compression algorithm, a much larger amount of signals needs to be sampled to cover all possible combinations. Considering, that two sides of the target area are sorting at the same time, and that slices of one row (or column) is selected at the same time, the number of sequences, in one channel, to move one row is then given by

$$n_{seq, row} = \left( \sum_{N=1}^{M-1} N \right)^2 = \frac{1}{4}(M^2 - M)^2. \quad (3.14)$$

The square comes from the fact, that for every frequency ramp on one side, a frequency ramp on the other side of the target area needs to be matched. A similar relation (replacing  $M$  by  $N$ ) is found for the number of sequences for the columns. Then, considering that the channels aren't independent, the total number of sequences is found by:

$$n_{seq} = M n_{seq,col} + N n_{seq,row}. \quad (3.15)$$

Taking also into account, that after the compression phase follows a pathfinding phase, it is already easy to see, that the memory requirement would greatly exceed the available memory of 4 GB on the spectrum M4i on a  $10 \times 10$  grid.

This means, in order to use the compression algorithm, the sequences need to be sampled on-the-fly. This is in general slow, compared to the sorting time if done on a CPU. However, it is possible to use parallelization of graphics processing units (GPUs). On a NVIDIA Geforce GTX 1080 Ti, 3584 cores are available, which can all sample part of a signal individually. This means for a sequence of 5 MB, 2 B per datapoint, about 700 calculations need to be made in sequence. Assuming only rectangles are sampled, this gives one comparison per sampled value and one insertion (into an array). At a clock speed of 1480 MHz [29], results in 0.5  $\mu$ s computation time, meaning only transfer speed from the GPU to the digitizer card is relevant. The transfer speed is then given from Table 3.3.1, adding 1.8 ms per move of one row (or column) of atoms.

Since one channel always has a fixed frequency, it is possible to use a VCO for this channel, meaning only half of the signals need to be sampled. Therefore, each move takes 0.9 ms to transfer from the GPU to the digitizer card and thus for the 60 transfers + 40 moves takes about 90 ms total.

## 3.4. Conclusion

It was shown how crossed AODs are used, in order to generate movable tweezers. As loading of atoms can only guarantee 50% filling, the tweezers are then used to sort atoms into the gaps, to guarantee a perfectly occupied grid, as long as the sorting happens faster than the lifetime of the atoms. Two different algorithms were discussed that move the atoms to their new locations, which are a pathfinding algorithm, moving single atoms and a compression algorithm, which is able to use parallelization, such that multiple atoms are

moved at the same time. It was shown that this approach reduces computation time of paths and sorting time of the atoms. Lastly, it was explained how the signals are generated using a digitizer card and the memory requirement for both algorithms were stated. It was shown, that as long as the grid is small enough, the pathfinding algorithm can be used with the digitizer card, as it has a smaller memory footprint. However, for a grid size of  $12 \times 12$  already, the memory of the digitizer card (Spectrum M4i.6680-x8) is not sufficient, such that on-the-fly calculations are inevitable and the compression algorithm, with smaller computation time, can be used.

## 4. State selective light shifts for spin-sensitive imaging

Being able to measure the spin of ground state potassium atoms in many-body quantum experiments gives insight into the full quantum state and thus being able to pinpoint the ground state on the Bloch sphere. In Rydberg dressing experiments [30–35], where the atom is in a ground state and fractionally in an excited Rydberg state, the spin can be used in a Ramsey sequence, in order to measure correlations [36]. This is, since the ground state atoms in a superposition of two spins, couple to the Rydberg state. To measure effects, such as Rydberg blockade [12, 37], and the resulting correlations, the superposition state acquires a phase on the Bloch sphere, which needs to be evaluated. This is currently achieved, by doing a projection measurement by removing one component out of the system.

With the new approach, it is possible to evaluate the spin species, by separating them in independent tweezers. A spin-sensitive tweezer array is then moved, and thus the atoms having this spin component follow this dipole potential. This creates a separation, and by evaluating the geometry from a fluorescence image, it is thus possible to find how the tweezer arrays were previously occupied. Measuring the spins this way, also means the atoms will not heat out during the process, and therefore the system can be reassembled and reused for further investigation.

The following chapter will discuss the setup in question in more detail, as well as the wavelength in use, in order to have tweezers sensitive to only one spin component. The new laser system is explained in detail, which includes a cavity for frequency stabilization, and therefore stability of the laser is discussed.

### 4.1. Approaches

Measuring the spin means in our experiment, to take a fluorescence image of the two ground states  $F = 1$  and  $F = 2$ . However, during imaging, the spins are mixed, such

that they can't be distinguished. As it was shown in Chapter 3, it is possible to move selected tweezers. Therefore two approaches are discussed in the following, both work by separating the two spins spatially, which requires finding ways of being sensitive to one specific ground-state spin. The first idea is using strong magnetic fields to increase the separation of the spin levels with the Zeeman effect. The second approach is using a state selective light shift, given by selecting a particular wavelength. This allows one spin component to be trapped, while the other will not see a trapping effect. In both applications, the idea is to trap one spin state in its own trap and physically move it away from the other. By taking an image, it is then possible to map positions to spins and therefore find out which tweezers contained which spin species. Moving the spin-sensitive tweezers back into its original position, the initial system is reassembled and new measurements can be taken with more information.

#### 4.1.1. Zeemann induced potential separation

Although the spin levels are too close in energy space, to address them with imaging lasers, having a position dependent potential, that is different for each spin state, is enough to spatially separate them. One way of achieving this, is by applying magnetic fields. In 1896, Pieter Zeeman wrote about how magnetic fields were affecting spectroscopy of atoms [38]. From this followed the Zeeman effect, which explains how spectral lines of atoms are split and shifted when applying magnetic fields. This can be calculated perturbatively [39], by modelling the atom as a magnetic dipole. In analogue to the classic description of magnetic dipoles, this gives an energy  $V_M$  depending on the magnetic field  $\mathbf{B}$ :

$$V_M = -\mu \mathbf{B} \quad (4.1)$$

and is then the perturbation in the total Hamiltonian  $H = H_0 + V_M$ . The magnetic moment  $\mu$  contains contributions from nuclear and electron spin, which then give direction and length of the magnetic dipole. The energy associated with the perturbation evaluates to

$$E_z = B_z \mu_B (g_l m_l + g_s m_s) . \quad (4.2)$$

It has contributions from the nuclear spin ( $g_l m_l$ ) and electron spin ( $g_s m_s$ ) and depends on the Bohr magneton  $\mu_B$ . The magnetic quantum numbers  $m_i, i \in \{l, s\}$  depend on the value of the associated quantum numbers, which are the orbital angular momentum  $L$  and electron angular momentum  $S$ , such that  $m_l \in \{-L, -L + 1, \dots, L - 1, L\}$  and  $m_s \in \{-S, -S + 1, \dots, S - 1, S\}$ . This means, not only is the hyperfine state shifted by the magnetic field, it is also split into more energy sublevels. However, a complete description of the energy shift, needs to integrate the shifts of the hyperfine levels, which has been done in the Breit-Rabi model [40].

Figure 4.1 gives an illustration of how the two spin components  $F = 1$  and  $F = 2$  in the potassium ground state are affected due to a magnetic field. Visible is a splitting of the spin-states into sublevels. In order to maximally separate the spin states, the  $F = 1$  spin would be pumped into the  $m_F = 1$  state, and consequently,  $F = 2$  into the  $m_F = 2$  state.

Using this, the idea is to create a position dependent trap for the two spin-states. To do this, we need to note, that from the figure, the  $F = 1, m_F = 1$  state has a negative slope, while the  $F = 2, m_F = 2$  state has a positive slope. This means, simply by generating a magnetic field ramp, the atoms in different spin states, will see a position dependent energy  $V_{mag}$ . Since the atoms are trapped inside optical tweezers, the potential given by the dipole force is [41]:

$$V_{dip}(r) = -\frac{\pi c^2 \Gamma}{2w_0^3 \Delta} I(r), \quad (4.3)$$

where  $\Gamma$  is the line width of the transition, in this case the D2 line,  $\Delta$  the detuning,  $w_0$  the resonance frequency and  $I(r)$  the intensity of the laser beam. By applying the magnetic field gradient, the atoms see a total potential  $V(r)$ :

$$V(r) = V_{dip}(r) + V_{mag}(B(r)), \quad (4.4)$$

where the position dependence was explicitly noted. This way, the potential minimum, which was originally just given by the dipole trap, is now shifted in the direction of the potential induced by the Zeeman effect. Thus, the two spin states will see different potentials, which are shifted in position space with respect to each other. However, numerical calculations of the potential minimum show that the shift is too small in order to spatially separate the atoms. For this, it is assumed, the atom is trapped on the D2-line and the laser

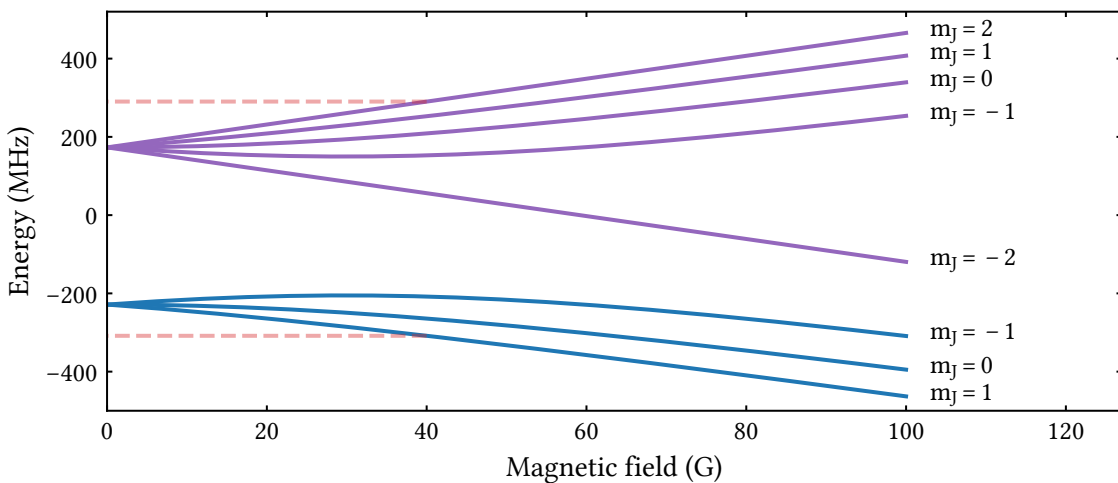


Figure 4.1.: The spectrum of ground state potassium is split into magnetic sublevels and shifted depending on a magnetic field applied to the atoms. Shown are two spin states  $F = 1$  in blue and  $F = 2$  in purple, relative to the ground state energy of  $4\text{S}_{1/2}$ .

power is  $1\text{ }\mu\text{W}$ , where the spatial separation is favorable towards lower laser powers. Moreover, the magnetic field gradient is set to  $B(r) = 40\text{ G cm}^{-1}$ , the maximum possible in our experiment. This gives a separation of  $\Delta x = 2.1\text{ nm}$ , which is much less than typical beam waists of  $w = 1\text{ }\mu\text{m}$ . These results are further illustrated in Figure 4.2.

The parameters used in the calculations are already on the optimistic end, which leads to the conclusion that this approach only works when very high magnetic fields are applied. Simulations show, that applying a magnetic field slope of  $B = 4000\text{ G cm}^{-1}$  results in a separation of  $0.2\text{ }\mu\text{m}$ . Luckily, there is another approach, which works by using only the light from frequency stable lasers, which is discussed in the following.

#### 4.1.2. Utilization of state selective light shifts

There is another effect that affects the energy of the spin states, similar to the Zeeman effect, in which electrical fields also shift and split energy levels [42, 43]. Under the influence of modulated electrical fields, such as coherent laser light, the effect is called AC Stark shift or simply light shift.

They are calculated in the semiclassical picture, where the light is treated classically and the atom is quantized. Moreover, in a simplified approach, the atom can be treated as a

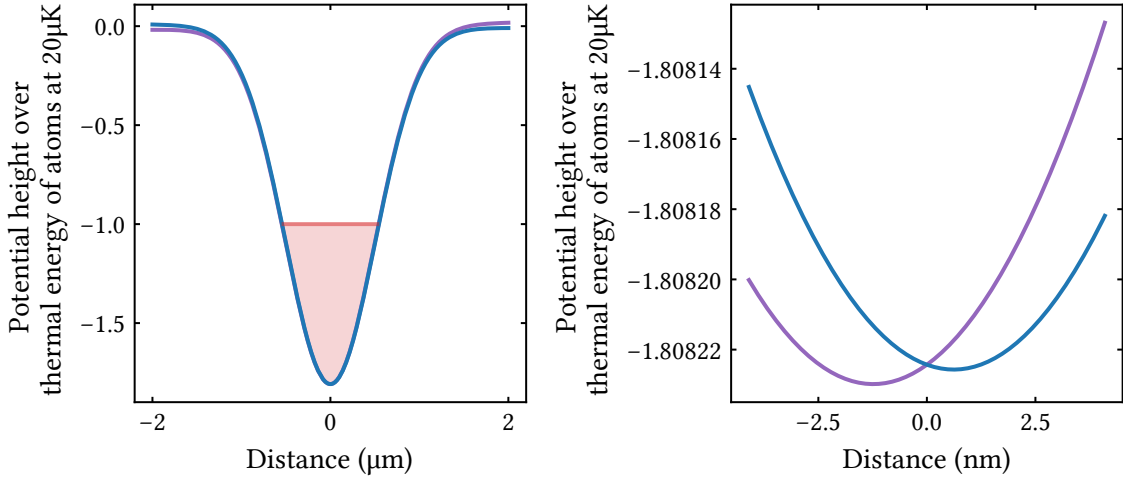


Figure 4.2.: Two spin species are subject to a dipole trap under the influence of a magnetic field gradient. The  $F = 1, m_F = 1$  and  $F = 2, m_F = 2$  states are colored in purple and blue respectively. The parameters for the trap are given in the text. Also shown is the energy of the atom as a red area. The zoomed in diagram on the right shows the separation of the two potentials, which is on the nanometer scale.

two-level system, when light is mostly resonant to a single excited state. Therefore, the electric field of the light and the state of the atom are written respectively as:

$$\mathbf{E}(\mathbf{r}, t) = \epsilon E_0 \cos(\mathbf{k}\mathbf{r} - \omega_L t) \quad (4.5)$$

$$|\Psi\rangle = c_g(t)|g\rangle + c_e(t)|e\rangle. \quad (4.6)$$

Here,  $\epsilon$  is the electric field vector and  $E_0$  its strength,  $\mathbf{k}$  and  $\omega_L$  are the wave vector and frequency of the field respectively. The state of the two-level atom changes with time, given by the ground and excited state probabilities  $|c_g(t)|^2$  and  $|c_e(t)|^2$ . Moreover, the transition from the ground to the excited state has a resonance at  $\omega_0$  and therefore the difference between the light frequency and the resonance is called the detuning,  $\Delta = \omega_L - \omega_0$ . The coupling between the electric field and the atom can be calculated from the dipole interaction and is simply  $V_I = -\mu\mathbf{E}$ , given the dipole operator  $\mu = -e\mathbf{r}$ . In this two-level system, where the atom is constantly driven by the electric field, the populations oscillate, however due to spontaneous emission, which can't be neglected, the excited state population will decay with time. This decay is calculated in [44] and the result is:

$$\Gamma = \frac{w_0^3}{3\pi\epsilon_0\hbar c^3} |\langle g|\boldsymbol{\mu}|e\rangle|^2. \quad (4.7)$$

To calculate the energy shift the states experience, perturbation theory can be applied in case the detuning is large [45], which to second order is in general:

$$\Delta E_i = \sum_{j \neq i} \frac{|\langle j|V_I|i\rangle|}{\epsilon_i - \epsilon_j} \quad (4.8)$$

Therefore, in the two-level system, the sum vanishes and the dipole matrix element  $\langle e|\boldsymbol{\mu}|g\rangle$  can be replaced with the decay rate from Equation 4.7 and therefore:

$$\Delta E_{\pm} = \pm \frac{|\langle e|\boldsymbol{\mu}|g\rangle|^2}{\Delta} |E^2| = \pm \frac{3\pi c^2}{2\omega_0^3} \frac{\Gamma}{\Delta} I \quad (4.9)$$

where the relation  $I = 2\epsilon_0 c |E|^2$  was used. The plus and minus sign of the energy shift refer to the excited and ground states respectively and it can be seen, that these shifts only depend on the light field. The two-level system is only a simplification and in a more complete scenario, contributions from all excited states need to be summed up. Moreover, for large laser powers, coupling to the nuclear spin has to be considered, resulting in the hyperfine splitting of the energy levels [45]. This results in the light shifts seen in Figure 4.3, for the two spin states,  $F = 1$  and  $F = 2$  for the potassium atoms in the experiment.

Due to the light shifts, the atoms see an induced potential, given by the energy of the state. Therefore, the two spins can be spatially separated, when one component sees a potential, where the other one does not. This is easy to see in Figure 4.4, where the light shifts for the two spin states are given as a function of wavelength of the laser for circularly polarized light. We can see, that at 768.40 nm, the  $F = 2$  state is trapped, while the  $F = 1$  component does not see a light shift, which makes the atom with this spin transparent to the light.

In the experiment then, the light is produced as optical tweezers using AODs as discussed in Chapter 3 and mapped over the SLM tweezers. To transfer the atoms into the spin-selective tweezer, the resulting trap has to be much deeper than the initial tweezers. These have a power of  $\approx 15$  mW, but are highly detuned to the excited state on the D2 line at a wavelength of 1064 nm. Moreover, high scattering rates will heat the atoms out of the

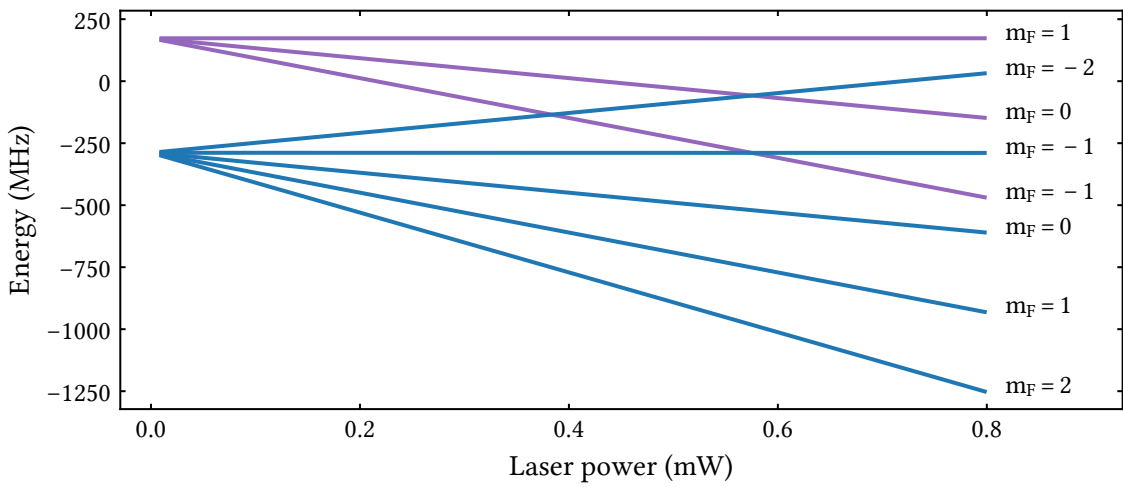


Figure 4.3.: The spin levels are split up due to the AC Stark shift from the laser illuminating the atoms. Shown are the ground states with  $F = 1$  in purple and  $F = 2$  in blue. The laser has a wavelength of 768.40 nm and positive circular polarization.

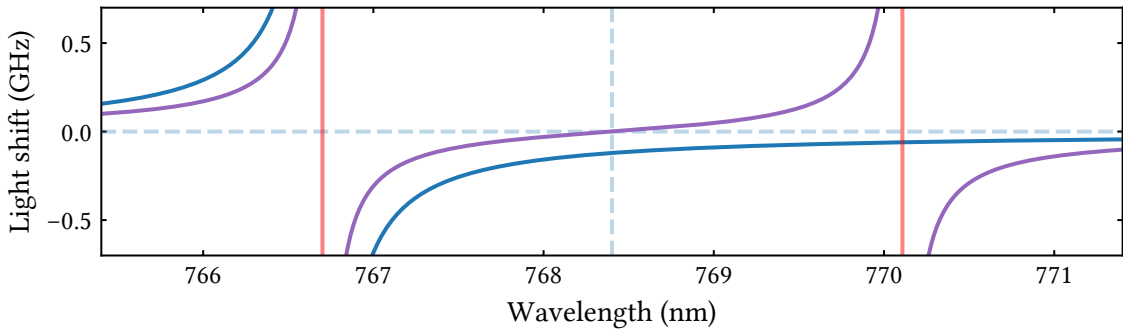


Figure 4.4.: The light shift of the  $F = 1, m_F = 1$  (purple) and  $F = 2, m_F = 2$  (blue) states against wavelength for a laser power of 0.1 mW and positive circular polarization. At 768.40 nm, the  $F = 1$  component is transparent to the laser, therefore making it possible to trap only the  $F = 2$  state.

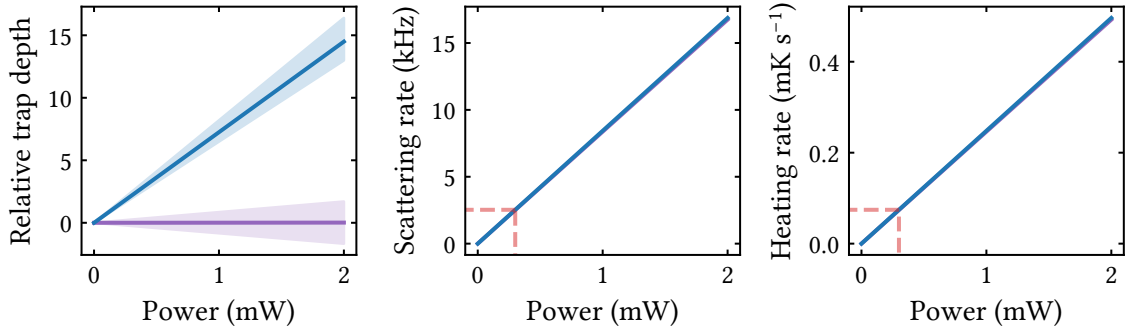


Figure 4.5.: On the left, the relative trap depth between the spin-selective tweezer and the SLM tweezer is shown as a function of the spin-tweezer laser power. For the  $F = 1, m_F = 1$  (purple) and  $F = 2, m_F = 2$  (blue) state, only one state is trapped. Already at 0.3 mW power, the spin tweezer is more than 2 times deeper than the SLM tweezer. The shaded area is for reference if the laser is shifted by  $\pm 100$  GHz. The middle plot shows the scattering rate of the tweezer as a function of laser power, where both spin states scatter practically the same amount of photons. As a guide to the eye, the 0.3 mW power is shown as a dashed red line. In the same vein, the right plot shows the heating rate inside a harmonic potential.

trap and therefore, both of these quantities have been verified to be compatible with the experiment and are given in Figure 4.5. The trap depth of the spin-selective tweezer is almost twice as deep as the SLM tweezer for a laser power of  $P = 300 \mu\text{W}$ , when the trap depth of the SLM tweezer is  $\approx 1 \text{ mK}$ . At this point, the scattering rate is  $\Gamma_{sc} = 2.5 \text{ kHz}$  or less than three photons per millisecond. Therefore, if the move happens during this time, almost no photons are being scattered. Moreover, a Raman sideband cooling technique that is implemented in the experiment [46] allows to cool atoms even further, therefore trap depths can be reduced by at least a factor of ten, which reduces scattering over one millisecond to less than one. To verify, that heating is not an issue, the heating rate due to dipole traps has been calculated [45] and is shown as a function of the laser power in Figure 4.5 as well. Consequently, using the AC-Stark shift in order to spatially separate the atoms is a viable approach to do spin-selective imaging.

## 4.2. Setup

We have seen, how light shifts can be used to trap a single spin species. Doing so, it is possible to spatially separate and image them onto a camera. However, it is necessary to have a stable laser at 768.40 nm. The following section highlights the steps in order to build

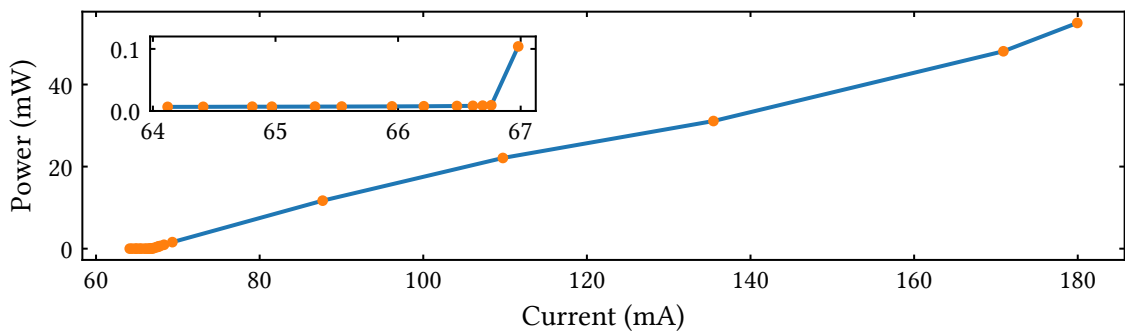


Figure 4.6.: Shown is the laser threshold for the home-built laser, driven with a Thorlabs LDC205C current controller. The power was measured using a Thorlabs PM100D power meter and the Thorlabs S121C sensor.

such a laser system, which includes setting up a cavity and a Pound Drever Hall (PDH) lock, that frequency stabilizes the system. The laser is then coupled into the same setup as in Chapter 3, allowing to generate acousto-optically deflected, spin-sensitive tweezers, allowing to move the spin state in space.

#### 4.2.1. Laser classification

The laser classified in the following is a homebuilt model, the design of which is given in Appendix A. It has room for a laser diode, whose light is collimated, filtered and reflected through a partially reflective mirror, which also serves as the output of the housing. The laser diode (Eagleyard EYP-RWE-0760-02010-1500-SOT12-0000) used, is tunable in the range from 752 nm to 772 nm with a maximum power of 80 mW. Since the diode is also used as the active medium, the cavity simplifies to being just a mirror, that reflects back into the diode and transmits part of the light out of the laser casing.

The laser power is classified as a function of current supplied to the laserdiode. Beyond the laser threshold, the power is linear with current and the diagram for the model built here is given in Figure 4.6.

#### 4.2.2. Beam setup of spin-selective laser

Now that there is a laser, the beam path in order to have a laser for spin-selective imaging can be set up. For this, two parts of the laser are split and coupled into fibers. One is used for monitoring of the wavelength, which will give an indication, if the frequency is

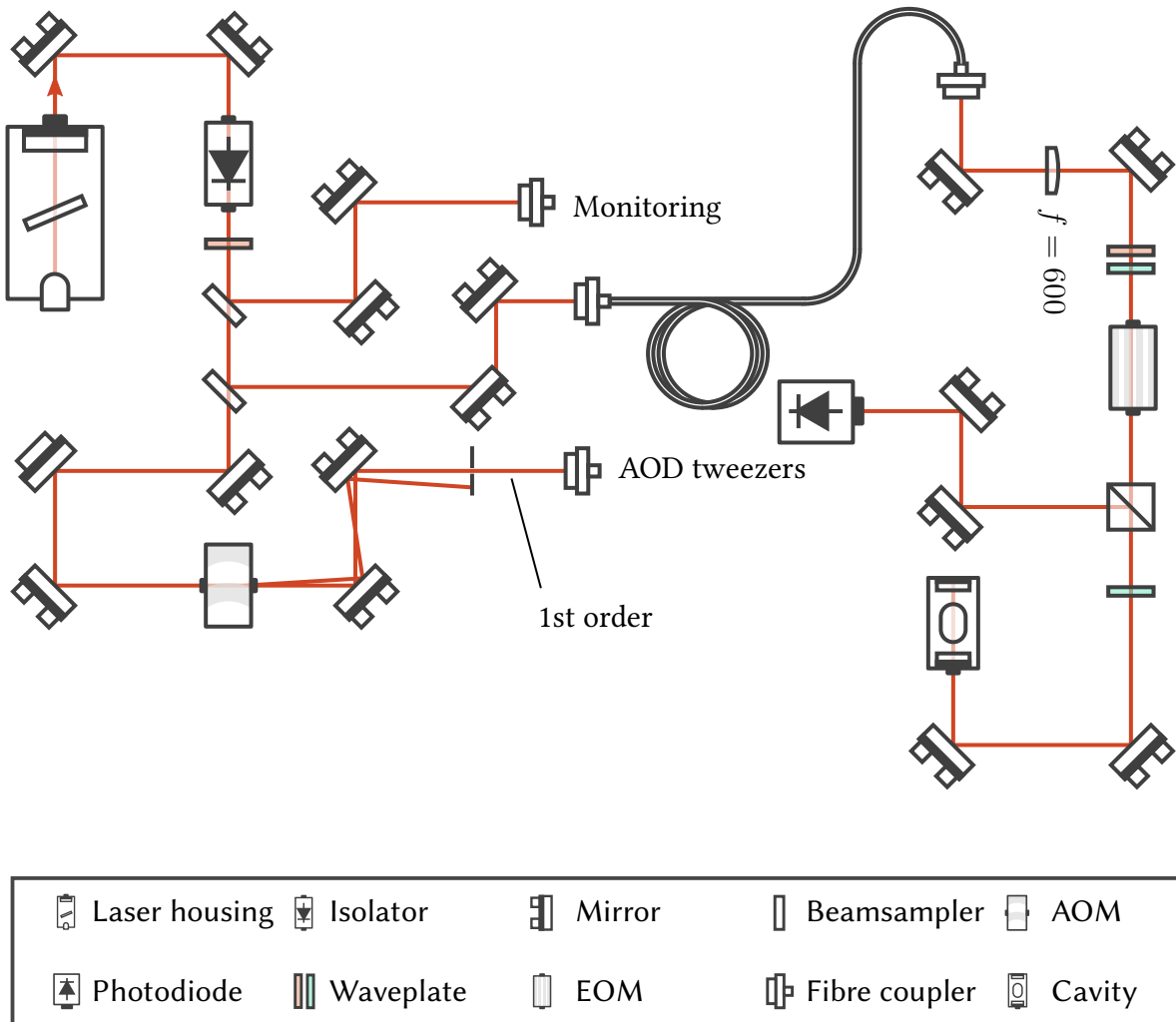


Figure 4.7.: Shown is the setup, in order to prepare the spin-sensitive tweezer for the experiment. The laser first passes an isolator, in order to protect the laser cavity from reflections. It is then split into two paths for monitoring and frequency stabilization. An AOD is used to switch the light on and off for the experiment.

currently locked or not. The second part will go to the cavity, allowing to actually perform the frequency stabilization. The full beam path is shown in Figure 4.7.

The main path is then coupled into a fibre, going towards the AOD discussed previously. However, the beam needs to be turned on and off at certain times during the experiment, for this, it first passes through an AOM and finally a shutter to block any leftover stray light. As shown previously, in 3.1.2, the light coming out of the fibre is then intensity stabilized and coupled into the AOD, which can be programmed to move the spin-sensitive tweezers.

### 4.2.3. Cavity classification

The laser has been built and characterized and can be coupled into the AOD, in order to generate movable tweezer for spin-selective imaging. However, the process requires a stable frequency at 768.40 nm. As a matter of fact, not only are there resonances at 766.7 nm and 770.1 nm, this spin-selecting procedure works by requires that one spin state is completely transparent to the laser light, in terms of seeing a dipole potential. In order to have the laser emit a stable frequency, a piezo tunes the position of the mirror inside the laser cavity based on an input signal. This way, the length of the cavity, and therefore the standing wave, can be selected. However, pressure and temperature can both affect the mirror, and therefore there needs to be a system in place, to compensate for these factors.

Consequently, it is necessary to have a device, that measures the instability, and feeds back a signal to the piezo. In order to do so, a part of the laser is split off and sent into a stable cavity. The light that has passed the cavity is measured using a photodiode and it is then possible to measure resonances of this cavity. With the PDH method, an error signal is generated, that gives a feedback to the piezo. This generates a feedback loop, which is stable when the error signal is at a minimum. The process has been used and described in the experiment before [18]. The error signal recorded for this specific setup was recorded and is given in Chapter C.

The stable cavity in place for locking the laser frequency is made from a ultra-low expansion (ULE) glass, that has two mirrors attached to it. The material is not explicitly necessary, however the full extent of this specific ULE couldn't be used anymore, as only one side has the mirror contacted, while the other mirror is glued. Therefore, due to the glue, this cavity is still prone to some wavelength drifts, induced by temperature expanding and compressing the material. This specific application can deal with these instabilities and therefore the glass was recycled for this setup. In order to stabilize the cavity against temperature fluctuations, it rests in a copper housing. This copper housing further rests in a stainless steel container. This container is then evacuated with a vacuum pump, which stabilizes the cavity against pressure fluctuations. A picture of the cavity is given in Appendix B.

In order to quantize the stability this cavity can provide, the frequency drift is measured. However, at 768.40 nm, the frequency is in the hundreds of terahertz, which is difficult to measure conventionally. However, by superimposing a reference laser onto the spin-laser, that has a very stable frequency, it is possible to measure the beat note. Mathematically, this means adding two sine-signals together:

$$\sin(2\pi f_1 t) + \sin(2\pi f_2 t) = 2 \sin\left(2\pi \frac{f_1 + f_2}{2} t\right) \cos\left(2\pi \frac{f_1 - f_2}{2} t\right), \quad (4.10)$$

where  $f_1$  and  $f_2$  are the frequencies of the reference and spin-laser respectively.

This relation turns two modulations, which have the frequencies added and subtracted. The first one still can't be resolved, however if the difference frequency is low enough, it is possible to see it on a spectrum analyzer. This means, the frequency of the "unstable" laser was first matched to the stable laser, such that the difference frequency was at least in the Megahertz regime. Then, it is possible to observe the drift of the cavity, which is the change in frequency with time. This usually happens due to temperature drifts affecting the cavity. The measurement was taken over several days and recorded as in Figure 4.8. Close to the end of the measurement, the drift was at a minimum of around 33 MHz per day, which is well within the limits, which can be verified with Figure 4.5. There, a shift of 100 GHz is shown as the shaded area and therefore it would take the cavity 30 days to drift to just one percent within this area. However it is important to note, that ULE glass has generally much lower drifts, on the order of kilohertz per day [47]. This means, the glue on one side of the glass cavity is the limiting factor for these drifts and the only way to improve on this, is to replace the ULE glass.

With the cavity in place, all building blocks are there in order to separate spins of ground state potassium atoms. This means, the frequency stability given by the cavity locks the laser and makes it possible to position it close to the magic wavelength, where only one spin state sees a trap. By coupling the beam into the crossed AOD, each atom can be addressed and moved individually and an image of the spins can be acquired, while simultaneously keeping the atoms in the trap.

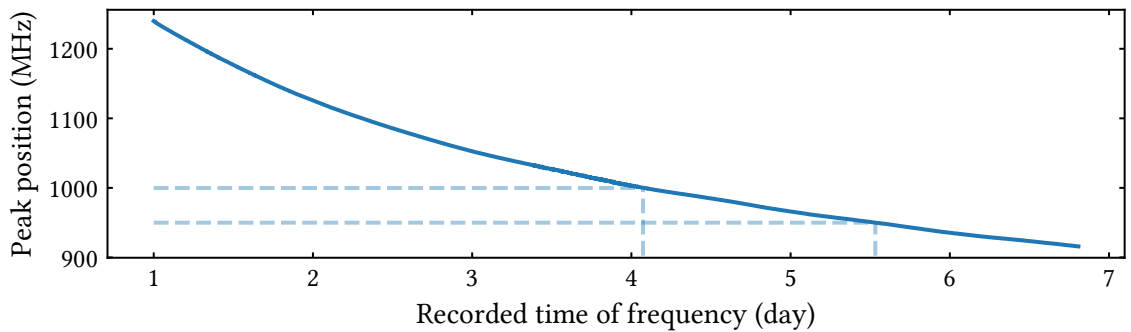


Figure 4.8.: The cavity drift was recorded over six days by doing a beat measurement with a reference laser. Horizontal lines show 50 MHz difference at the end of the measurement, where temperature and pressure has stabilized. From this it can be seen, that the drift is on the order of 33 MHz per day.



## 5. Conclusion and Outlook

This thesis discussed setups related to optical tweezer arrays in a Potassium-39 experiment. It was shown, how using a Pockels cell improves a current setup for loading atoms into SLM tweezers. With the new implementation, the duty cycle of the dipole traps during the chopping sequence can be increased, effectively improving the power available for every single tweezer. This also opens up the possibility of increasing the number of tweezer, as the trap depth available currently can then be distributed across a larger area. The discussion of sorting atoms followed, which solves the problem of only having 50% of sites occupied due to parametric heating. The solution requires moving atoms into unoccupied sites, which can be implemented using a pathfinding algorithm. As an alternative, a new algorithm was proposed, that uses parallelization and a digitizer card to move multiple atoms at the same time. The chapter was concluded by comparing the efficiency of the algorithms and by highlighting the requirements when using the digitizer card. The third setup then discussed an approach of doing spin-selective imaging, which will be useful in experiments involving Rydberg dressed states, as they are mostly ground states, but of unknown spin. For this, the spin states are spatially separated by using spin selective light shifts induced by a frequency stabilized laser. The laser system was built and characterized, and a stable cavity with a feedback loop to the laser for frequency stabilization was described. It is then coupled into the same crossed AODs used for the sorting, allowing to move atoms (and therefore the spin states) apart.

Shown were ways of improving the current state of the experimental setup. Moreover, there are applications beyond the scope of the current system in place. As was shown, the EOMs presented here also have faster repetition rates than the AOMs used currently. Apart from loading, it is then possible to drive faster pi-pulses in the experiment, or start doing Floquet engineering [48], which requires periodic driving of atoms. For sorting, being able to fill every site in an atomic array opens the door to manybody Rydberg effects. This allows for example to model antiferromagnets in an Ising-like system [49] and measure correlations without the need of heavy post-selection of data. It was motivated, how spin-selective imaging reduces cycle times, which ultimately leads to being able to take more statistics. This is a requirement to measuring entanglement entropies, for example Rényi

entropies [50] in a quantum information application of the experiment. Conclusively, the setups that were built over the course of this thesis offer a way to explore manybody Rydberg effects with high cycle times and high fidelity.

## A. Linear laser design

The linear laser was designed by Nikolaus Lorenz and is used in multiple parts of the experiment.

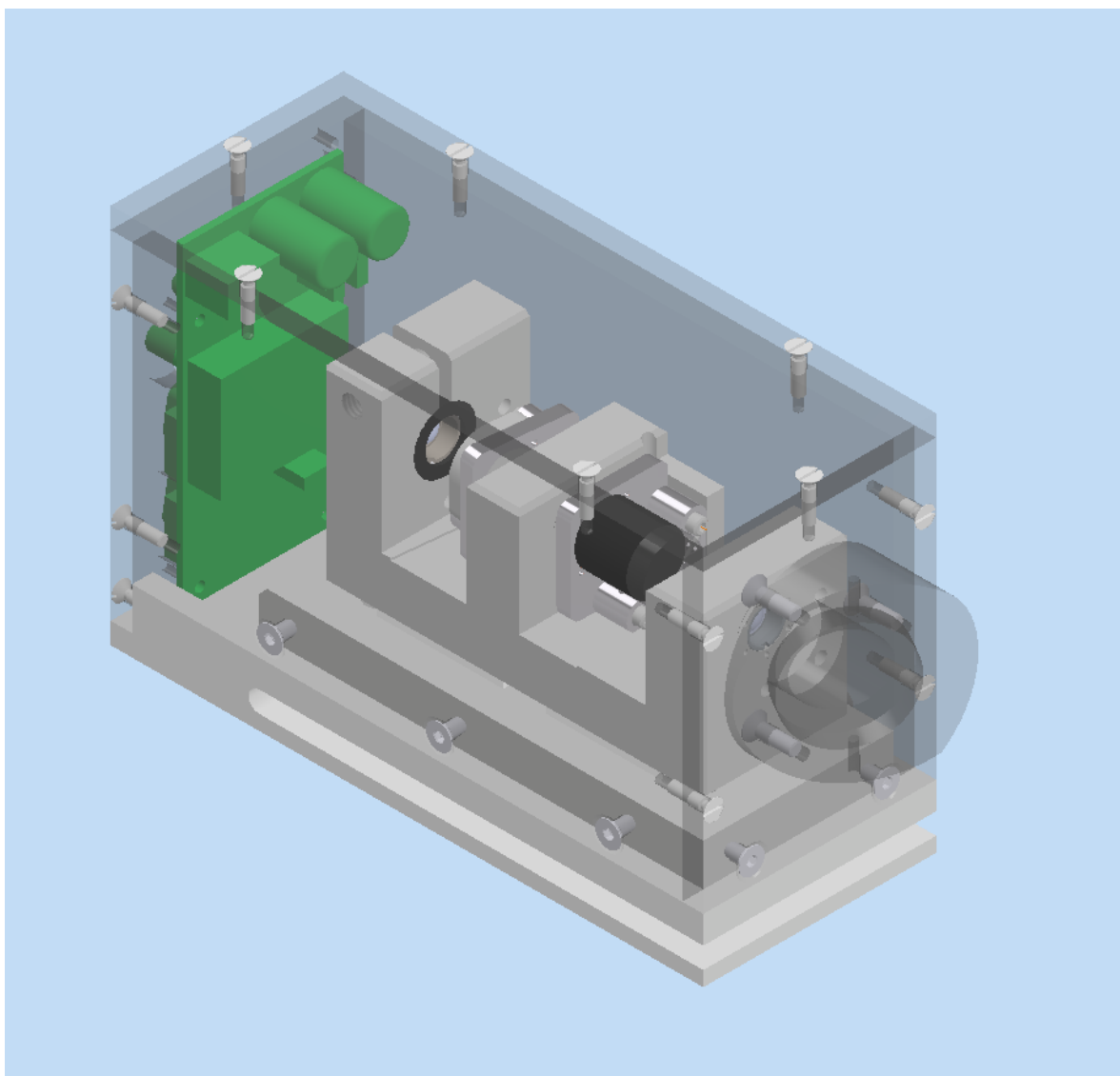


Figure A.1.: The laser casing used for the spin-sensitive tweezer. It consists of a diode, filter, lens and a mirror.



## **B. Cavity for frequency stability of spin-sensitive tweezer**

A special cavity was built in order to stabilize the spin-sensitive tweezer against its frequency. The outer housing is made of stainless steel and can be evacuated using the flange in the back. The cavity is a ULE spacer, resting on a copper block, which should absorb most temperature instabilities. The spacer is surrounded by Viton rings, to prevent it from damage against direct contact with the copper block. Not visible are peek spacer between the copper block and steel casing, which isolate both parts from each other. A picture of the cavity is given below, in Figure B.1.

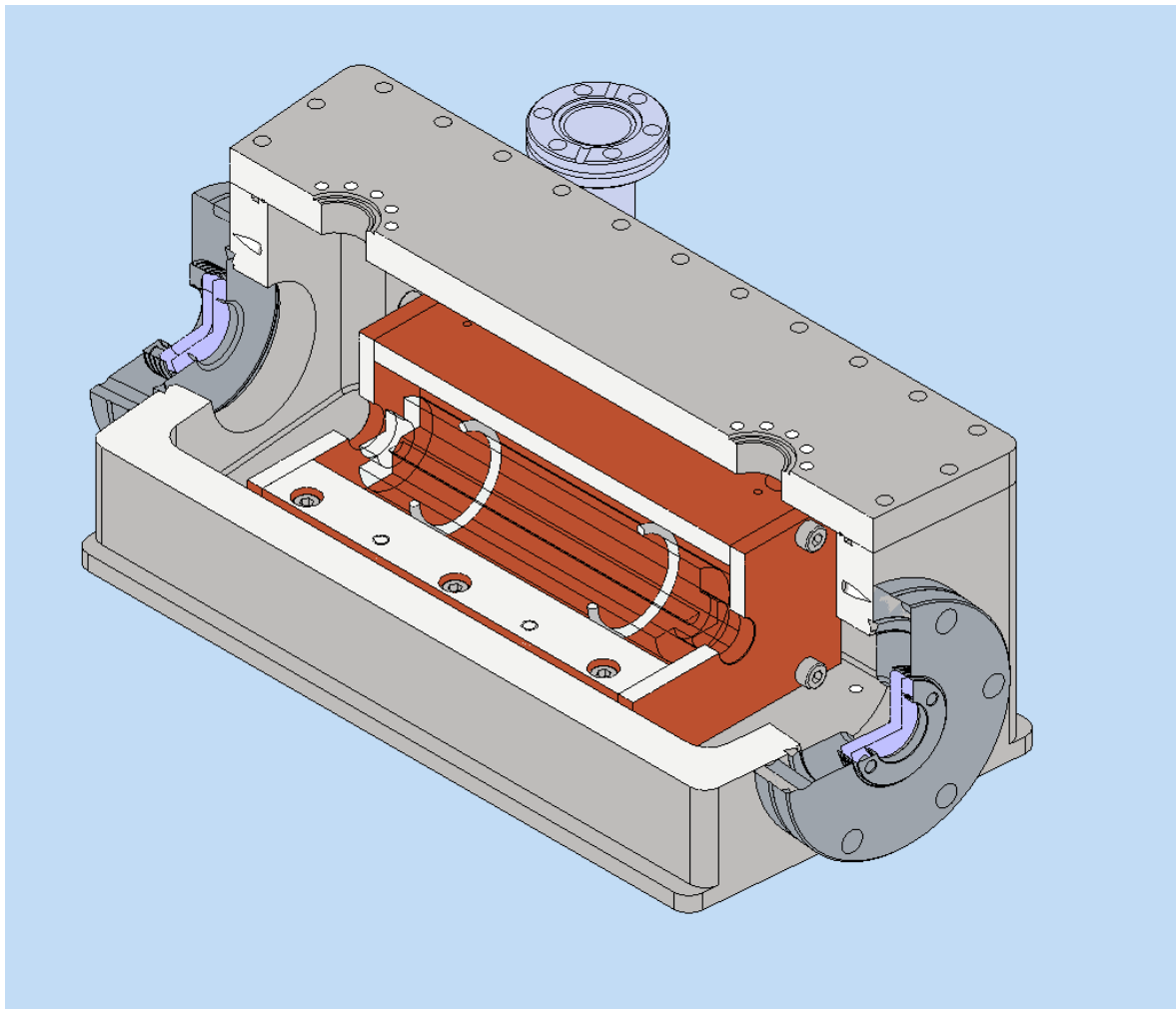


Figure B.1.: The cavity used for frequency locking the spins-sensitive tweezer.

## C. PDH lock of cavity

Given below is the PDH locking signal retrieved, when scanning through the cavity.

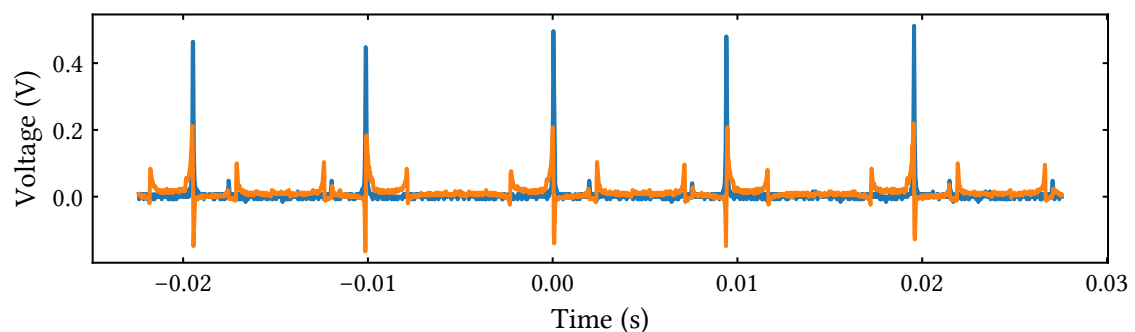


Figure C.1.: The PDH locking signal (orange) and the transmission signal of the cavity (blue).



# Acknowledgements

Working on this master's project has been a fantastic experience and I want to thank everyone involved. I am very thankful for the possibility of exploring nature in the most interesting way. There are still some exciting years ahead of me that I am looking forward to, however reaching this milestone is a great achievement that I am very proud of.

For the people who have supported me in reaching this step, I am very thankful. In this vein, my family is first on the list, as they have encouraged me to proceed on this path and have always supported me no matter my choices. I also want to thank Karsten at the Max Planck Institute for Quantum optics, who I worked with prior to this thesis. He has helped me become familiar with the institute and provided a workplace I felt comfortable with, while encouraging me to work here on a thesis. Then of course I want to thank all people involved in the Potassium group, Lorenzo, Niko, Lea and Philip with whom I have enjoyed working with very much for the last year. Thank you Christian, for allowing me to be part of this group, for the fruitful discussions and for supervising this thesis. I'm looking forward to the next few years with everyone.

And finally, thank you Meli, for being there for me during every part of the study and helping me go through all the difficult times.



# Bibliography

1. Brewer, S. M. *et al.* Al+ 27 Quantum-Logic Clock with a Systematic Uncertainty below 10–18. *Physical Review Letters* **123**, 33201 (2019) (cit. on p. 1).
2. Anderson, M. H., Ensher, J. R., Matthews, M. R., Wieman, C. E. & Cornell, E. A. Observation of bose-einstein condensation in a dilute atomic vapor. *Collected Papers of Carl Wieman* **269**, 453–456 (1995) (cit. on p. 1).
3. Davis, K. B. *et al.* Bose-Einstein Condensation in a Gas of Sodium Atoms. *Phys. Rev. Lett.* **75**, 3969–3973 (1995) (cit. on p. 1).
4. Schauß, P. *et al.* Crystallization in Isingquantum magnets (2015) (cit. on p. 1).
5. Boll, M. *et al.* Spin- and density-resolved microscopy of antiferromagnetic correlations in Fermi-Hubbard chains. *Science* **353**, 1257–1260 (2016) (cit. on p. 1).
6. Bakr, W. S., Gillen, J. I., Peng, A., Fölling, S. & Greiner, M. A quantum gas microscope for detecting single atoms in a Hubbard-regime optical lattice. *Nature* **462**, 74–77 (2009) (cit. on p. 1).
7. Sherson, J. F. *et al.* Single-atom-resolved fluorescence imaging of an atomic Mott insulator. *Nature* **467**, 68–72 (2010) (cit. on p. 1).
8. Lee, W., Kim, H. & Ahn, J. Three-dimensional rearrangement of single atoms using actively controlled optical microtraps. *Optics Express* **24**, 9816 (2016) (cit. on pp. 1, 15)
- .
9. Barredo, D., De Léséleuc, S., Lienhard, V., Lahaye, T. & Browaeys, A. An atom-by-atom assembler of defect-free arbitrary two-dimensional atomic arrays. *Science* **354**, 1021–1023 (Nov. 2016) (cit. on pp. 1, 15).
10. Endres, M. *et al.* Atom-by-atom assembly of defect-free one-dimensional cold atom arrays. *Science* **354**, 1024–1027 (Nov. 2016) (cit. on pp. 1, 15).
11. Norcia, M. A., Young, A. W. & Kaufman, A. M. Microscopic Control and Detection of Ultracold Strontium in Optical-Tweezer Arrays. *Physical Review X* **8**, 41054 (2018) (cit. on p. 1).

## Bibliography

---

12. Urban, E. *et al.* Observation of Rydberg blockade between two atoms. *Nature Physics* **5**, 110–114 (2009) (cit. on pp. 1, 39).
13. Kiffner, M., O'Brien, E. & Jaksch, D. Topological spin models in Rydberg lattices. *Applied Physics B: Lasers and Optics* **123**, 1–10 (2017) (cit. on p. 2).
14. Barredo, D. *et al.* Coherent excitation transfer in a spin Chain of three rydberg atoms. *Physical Review Letters* **114**, 1–5 (2015) (cit. on p. 2).
15. Labuhn, H. *et al.* Tunable two-dimensional arrays of single Rydberg atoms for realizing quantum Ising models. *Nature* **534**, 667–670 (2016) (cit. on p. 2).
16. Fan, R., Zhang, P., Shen, H. & Zhai, H. Out-of-time-order correlation for many-body localization. *Science Bulletin* **62**, 707–711 (2017) (cit. on p. 2).
17. Bernien, H. *et al.* Probing many-body dynamics on a 51-atom quantum simulator. *Nature* **551**, 579–584 (2017) (cit. on p. 2).
18. Hirthe, S. A Laser Setup for Two-Photon Rydberg Excitation of Potassium, Msc-thesis (2018) (cit. on pp. 2, 49).
19. Osterholz, P. Freely Configurable Holographic Trap Arrays for the Trapping of Single Atoms, Msc-thesis (2020) (cit. on pp. 2, 3, 21).
20. Salomon, G. *et al.* Gray-molasses cooling of 39K to a high phase-space density. *Epl* **104** (2013) (cit. on p. 3).
21. Hutzler, N. R., Liu, L. R., Yu, Y. & Ni, K. K. Eliminating light shifts for single atom trapping. *New Journal of Physics* **19** (2017) (cit. on p. 3).
22. Saleh, B. E. A. & Teich, M. C. *Fundamentals of Photonics* (John Wiley & Sons, Inc., New York, USA, Aug. 1991) (cit. on pp. 6, 16).
23. BME Bergmann. *Pockels Cell Driver Head* <https://web.archive.org/web/20200712183516/https://www.bme-bergmann.de/high-voltage-electronics/pockels-cell-driver-head/> (09/14/2020) (cit. on p. 12).
24. Cooper, A. *et al.* Alkaline-Earth Atoms in Optical Tweezers. *Physical Review X* **8** (Dec. 2018) (cit. on p. 15).
25. Barredo, D., Lienhard, V., de Léséleuc, S., Lahaye, T. & Browaeys, A. Synthetic three-dimensional atomic structures assembled atom by atom. *Nature* **561**, 79–82 (2018) (cit. on p. 15).
26. Fredman, M. L. & Tarjan, R. Fibonacci Heaps And Their Uses In Improved Network Optimization Algorithms, 338–346 (1984) (cit. on p. 24).

## Bibliography

---

27. Ohl de Mello, D., Birkl, G. & Walther, T. Rydberg interactions in a defect-free array of single-atom quantum systems (2020) (cit. on p. 25) .
28. Leseleuc, S. D. Quantum simulation of spin models with assembled arrays of Rydberg atoms (2018) (cit. on p. 34) .
29. NVIDIA. *Grafikkarten der GeForce 10-Serie* <https://www.nvidia.com/de-de/geforce/10-series/> (10/01/2020) (cit. on p. 37) .
30. Bouchoule, I. & Mølmer, K. Spin squeezing of atoms by the dipole interaction in virtually excited Rydberg states. *Physical Review A. Atomic, Molecular, and Optical Physics* **65**, 418031–418034 (2002) (cit. on p. 39) .
31. Pupillo, G., Micheli, A., Boninsegni, M., Lesanovsky, I. & Zoller, P. Strongly correlated gases of rydberg-dressed atoms: Quantum and classical dynamics. *Physical Review Letters* **104**, 3–6 (2010) (cit. on p. 39) .
32. Van Bijnen, R. E. & Pohl, T. Quantum Magnetism and Topological Ordering via Rydberg Dressing near Förster Resonances. *Physical Review Letters* **114**, 1–5 (2015) (cit. on p. 39) .
33. Glaetzle, A. W. *et al.* Designing frustrated quantum magnets with laser-dressed Rydberg atoms. *Physical Review Letters* **114**, 1–5 (2015) (cit. on p. 39) .
34. Zeiher, J. *et al.* Many-body interferometry of a Rydberg-dressed spin lattice. *Nature Physics* **12**, 1095–1099 (2016) (cit. on p. 39) .
35. Borish, V., Marković, O., Hines, J. A., Rajagopal, S. V. & Schleier-Smith, M. Transverse-Field Ising Dynamics in a Rydberg-Dressed Atomic Gas. *Physical Review Letters* **124**, 1–6 (2020) (cit. on p. 39) .
36. Zeiher, J. *et al.* Coherent many-body spin dynamics in a long-range interacting Ising chain. *Physical Review X* **7**, 1–6 (2017) (cit. on p. 39) .
37. Jaksch, D. *et al.* Fast quantum gates for neutral atoms. *Physical Review Letters* **85**, 2208–2211 (2000) (cit. on p. 39) .
38. Zeeman, P. Ueber einen Einfluss der Magnetisirung auf die Natur des von einer Substanz emittirten Lichtes. *Verhandlungen der Physikalischen Gesellschaft zu Berlin* (1896) (cit. on p. 40) .
39. Griffiths, D. J. *Introduction to Quantum Mechanics (2nd Edition)* 2nd ed. (Pearson Prentice Hall, 2004) (cit. on p. 40) .
40. Breit, G. & Rabi, I. I. Measurement of nuclear spin [10]. *Physical Review* **38**, 2082–2083 (1931) (cit. on p. 41) .

## Bibliography

---

41. Le Kien, F., Schneeweiss, P. & Rauschenbeutel, A. Dynamical polarizability of atoms in arbitrary light fields: General theory and application to cesium. *European Physical Journal D* **67** (2013) (cit. on p. 41).
42. Voigt, W. Ueber das Elektrische Analogon des Zeeman-effectes. *Annalen der Physik* **309** (1901) (cit. on p. 42).
43. Courtney, M., Spellmeyer, N., Jiao, H. & Kleppner, D. Classical, semiclassical, and quantum dynamics in the lithium Stark system. *Physical Review A* **51**, 3604–3620 (1995) (cit. on p. 42).
44. King, B. E. Angular Momentum Coupling and Rabi Frequencies for Simple Atomic Transitions. arXiv: 0804 . 4528 (2008) (cit. on p. 43).
45. Grimm, R., Weidemüller, M. & Ovchinnikov, Y. B. Optical Dipole Traps for Neutral Atoms. *Advances in Atomic, Molecular and Optical Physics* **42**, 95–170 (2000) (cit. on pp. 44, 46).
46. Thompson, J. D., Tiecke, T. G., Zibrov, A. S., Vuletić, V. & Lukin, M. D. Coherence and Raman sideband cooling of a single atom in an optical tweezer. *Physical Review Letters* **110**, 1–5 (2013) (cit. on p. 46).
47. Haindl, R. A Clock Laser System for Quantum Simulations with Ultracold Strontium Atoms, Msc-thesis. *Master thesis* (2019) (cit. on p. 50).
48. Oka, T. & Kitamura, S. Floquet engineering of quantum materials. *Annual Review of Condensed Matter Physics* **10**, 387–408 (2019) (cit. on p. 53).
49. Lienhard, V. *et al.* Observing the Space- and Time-Dependent Growth of Correlations in Dynamically Tuned Synthetic Ising Models with Antiferromagnetic Interactions. *Physical Review X* **8**, 1–17 (2018) (cit. on p. 53).
50. Wilde, M. M., Winter, A. & Yang, D. Strong Converse for the Classical Capacity of Entanglement-Breaking and Hadamard Channels via a Sandwiched Rényi Relative Entropy. *Communications in Mathematical Physics* **331**, 593–622 (2014) (cit. on p. 54).

# **Erklärung**

Hiermit erkläre ich, die vorliegende Arbeit selbständig verfasst zu haben und keine anderen als die in der Arbeit angegebenen Quellen und Hilfsmittel benutzt zu haben.

Munich, October 16, 2020

---

Signature